Ecological Informatics 83 (2024) 102814

Contents lists available at ScienceDirect

Ecological Informatics

journal homepage: www.elsevier.com/locate/ecolinf

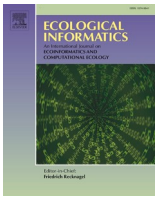

Spatio-temporal variability of turbidity derived from Sentinel-2 in Reloncaví sound, Northern Patagonia, Chile

Wirmer García-Tuñon [a,b,*], Elizabeth D. Curra-Sánchez [c,d,e], Carlos Lara [f,g], Lisdelys González-Rodríguez [c,d], Esther Patricia Urrego [h], Jesús Delegido [h], Bernardo R. Broitman [e,i]

[a] Programa de Magíster en Ecología Marina, Facultad de Ciencias, Universidad Católica de la Santísima Concepción, Concepción, Chile
[b] Data Observatory Foundation, ANID Technology Center No. DO210001, Santiago, Chile
[c] Facultad de Ingeniería y Negocios, Universidad de Las Américas, Sede Concepción, Concepción, Chile
[d] Núcleo de Investigación en Data Science, Facultad de Ingeniería y Negocios, Universidad de Las Américas, Santiago, Chile
[e] Instituto Milenio en Socio-Ecología Costera (SECOS), Pontificia Universidad Católica de Chile, Santiago, Chile
[f] Departamento de Ecología, Facultad de Ciencias, Universidad Católica de la Santísima Concepción, Concepción, Chile
[g] Centro de Investigación en Recursos Naturales y Sustentabilidad (CIRENYS), Universidad Bernardo O'Higgins, Santiago, Chile
[h] Image Processing Laboratory, Universitat de València, Paterna, Spain
[i] Departamento de Ciencias, Facultad de Artes Liberales, Universidad Adolfo Ibáñez, Viña del Mar, Chile

ARTICLE INFO

Keywords:
Remote sensing
Satellite algorithms
Ocean color
Aquaculture
Temporal patterns
Water quality monitoring

ABSTRACT

Turbidity is associated with the loss of water transparency due to the presence of particles, sediments, suspended solids, and organic or inorganic compounds in the water, of natural or anthropogenic origin. Our study aimed to evaluate the spatio-temporal variability of turbidity from Sentinel-2 (S2) images in the Reloncaví sound and fjord, in Northern Patagonia, Chile, a coastal ecosystem that is intensively used by finfish and shellfish aquaculture. To this end, we downloaded 123 S2 images and assembled a five-year time series (2016–2020) covering five study sites (R1 to R5) located along the axis of the fjord and seaward into the sound. We used Acolite to perform the atmospheric correction and estimate turbidity with two algorithms proposed by Nechad et al. (2009, 2016 Nv09 and Nv16, respectively). When compared to match-up, and *in situ* measurements, both algorithms had the same performance ($R^2 = 0.40$). The Nv09 algorithm, however, yielded smaller errors than Nv16 (RMSE = 0.66 FNU and RMSE = 0.84 FNU, respectively). Results from true-color imagery and two Nechad algorithms singled an image from the austral autumn of 2019 as the one with the highest turbidity. Similarly, three images from the 2020 austral autumn (May 20, 25, 30) also exhibited high turbidity values. The turbid plumes with the greatest extent occurred in the autumn of 2019 and 2020, coinciding with the most severe storms and runoff events of the year, and the highest turbidity values. Temporal trends in turbidity were not significant at any of the study sites. However, turbidity trends at sites R1 and R2 suggested an increasing trend, while the other sites showed the opposite trend. Site R1 recorded the highest turbidity values, and the lowest values were recorded at R5 in the center of the sound. The month of May was characterized by the highest turbidity values. The application of algorithms from high-resolution satellite images proved to be effective for the estimation and mapping of this water quality parameter in the study area. The use of S2 imagery unraveled a predictable spatial and temporal structure of turbidity patterns in this optically complex aquatic environment. Our results suggest that the availability of *in situ* data and the continued evaluation of the performance of the Nechad algorithms can yield significant insights into the dynamics and impacts of turbid waters in this important coastal ecosystem.

1. Introduction

Turbidity stands out as a key parameter to understand the health of marine and aquatic ecosystems worldwide. An increase in water turbidity is associated with the presence of suspended and/or dissolved material of natural or anthropogenic origin (Abirhire et al., 2020; Bilotta

* Corresponding author at: Facultad de Ciencias, Universidad Católica de la Santísima Concepción, Concepción, Chile.
E-mail address: wgarcia@magister.ucsc.cl (W. García-Tuñon).

https://doi.org/10.1016/j.ecoinf.2024.102814
Received 26 April 2024; Received in revised form 3 September 2024; Accepted 3 September 2024
Available online 5 September 2024
1574-9541/© 2024 The Authors. Published by Elsevier B.V. This is an open access article under the CC BY-NC-ND license (http://creativecommons.org/licenses/by-nc-nd/4.0/).

and Brazier, 2008; Grobbelaar, 2009; Smith, 2003). Water quality in coastal regions is of special concern; over a third of the global population inhabits the world's coastlines and depends on them to provide multiple ecosystem services, particularly in developing countries (Barragán and de Andrés, 2015). Turbidity in coastal marine and inner water systems can be influenced by algal blooms and suspended sediments. Similarly, overland surface runoff from rainfall events can carry colored dissolved organic matter (CDOM) or excess nutrients from agriculture, sewage, or animal husbandry among other anthropogenic compounds (Abirhire et al., 2020; Babin et al., 2003; Brando et al., 2015; Lee et al., 2015; Mendes et al., 2014; Potes et al., 2012; Saldías et al., 2012). As visible light (400–700 nm) strongly declines with depth, increased turbidity compresses the euphotic depth and curtails the energy available for photosynthesis (Cloern, 1987; Davies-Colley and Smith, 2001; de Castro Medeiros et al., 2015; Kirk, 1985; Pérez-Ruzafa et al., 2019; Zohary et al., 2009). On the other hand, water-clouding components and particulates facilitate the dispersion of contaminants by providing a vector for their transport, that can also precipitate and smother benthic communities (Alma et al., 2023; Anderson et al., 2012; Díaz et al., 2019; Gelda et al., 2013; Goldsmith et al., 2021; Quang et al., 2017; Soria et al., 2021; Vanhellemont and Ruddick, 2014). Thus, the threats to the well-being of coastal societies and ecosystems posed by changes in turbidity can be faced through scientific advances that help to accurately and dynamically estimate turbidity and its causes.

Methods for measuring turbidity *in situ* include indirect metrics, such as the Secchi disk depth (SDD), which directly measures water transparency and is inversely related to turbidity, or direct quantification using turbidimeters or nephelometers. These turbidity measurements are very accurate but they are chiefly manual procedures and require the intensive use of personnel. Hence, *in situ* techniques can be resource-intensive and consequently of limited spatial and temporal resolution (Alvado et al., 2021; Caballero et al., 2020; Delegido et al., 2019; Rodríguez-López et al., 2022; Sòria-Perpinyà et al., 2021; Zhan et al., 2022). Turbidity measurements are usually reported in Nephelometric Turbidity Units (NTU) and Formazin Nephelometric Units (FNU). Studies by Anderson (2005) and Dogliotti et al. (2015) indicated that there is no difference between the units in which turbidity is expressed (NTU and FNU), and both turbidity units are comparable or equivalent regardless of the instrument's technology used. Ocean color remote sensing currently provide direct estimations of water turbidity and other environmental variables over multiple spatial and temporal scales (Aragonés et al., 2016; Caballero et al., 2019; Caballero and Stumpf, 2020; Dickey et al., 2006; Khan et al., 2021). Multiple satellite missions now provide synoptic measurement of the properties and Optically Active Constituents (OACs) of water such as chlorophyll, CDOM, and suspended solids (SS), among others (Aavaste et al., 2021; Kuhn et al., 2019; Sòria-Perpinyà et al., 2022; Vantrepotte et al., 2012; Werdell et al., 2018). In this way, turbidity in water can be estimated through inherent and apparent optical properties (Inherent Optical Properties - IOPs and Apparent Optical Properties - AOPs, respectively), as well as through the OACs that are present in aquatic ecosystems (Budhiman et al., 2012; Dogliotti et al., 2015; Kirk, 1984; Soriano-González et al., 2022).

The waters of coastal zones are optically complex and known as Case 2 waters (Jerlov, 1957; Mélin and Vantrepotte, 2015; Morel and Gentili, 1993; Morel and Prieur, 1977). The turbidity of coastal waters is determined by the independent variation of OACs in the water (Aavaste et al., 2021; Babin et al., 2003; Odermatt et al., 2012; Uudeberg et al., 2019; Uudeberg et al., 2020; Vantrepotte et al., 2012). Generally speaking, the presence and concentration of OACs is determined by factors that influence both, IOPs and AOPs. According to Morel and Prieur (1977) and Mobley (2001, 2022), IOPs are defined as the physical determinants of how light interacts with water and allow us to understand the absorption and scattering of electromagnetic radiation as a function of its various constituents. IOPs are independent of the light field (absorption and scattering coefficients). Their variations are directly related to changes in the concentration, size distribution, and composition of OACs (Aavaste et al., 2021; Dickey et al., 2006; Werdell et al., 2018). On the other hand, AOPs were defined by Preisendorfer (1976), Morel and Gentili (1993), and Mobley (2001) as the optical properties of water that are influenced by the distribution of the angles of incidence and the amount of light and illumination available in the environment, together with the concentration of substances present in the medium. That is, AOPs vary depending on how the medium is illuminated (*i.e.*, radiance and reflectance) (Jerlov, 1957; Kirk, 1984; Mobley, 2001, 2022).

Empirical and semi-empirical algorithms from satellite imagery can be used to estimate water quality parameters (WQP) such as total suspended solids (SS), CDOM, chlorophyll-a concentration (Chl-a), and turbidity in different waters using the optical properties and OACs of water (*e.g.*, Z. Lee et al., 2002; Nechad et al., 2009, 2010; Phuoc Hoang Son et al., 2013; Dogliotti et al., 2015; Balasubramanian et al., 2020; Magrì et al., 2023). In this way, the products derived from remote sensing allow the continuous monitoring of WQP in the ocean and coastal zone over time and the study of their association with different environmental drivers (Werdell et al., 2018). However, understanding the drivers of WQP and how they change under emergent anthropogenic threats requires an accurate assessment of the quality and bias of satellite estimates (Pahlevan et al., 2021; Sòria-Perpinyà et al., 2021; Vanhellemont, 2019; Vanhellemont and Ruddick, 2016, 2021).

Recently, the use of high spatial, temporal, and spectral resolution images from multispectral optical sensors such as Landsat and Sentinel-2 (S2) or their combination, has become a valuable tool for studying the dynamics of water transparency (Caballero et al., 2022; Jiang et al., 2024; Khan et al., 2021; Kuhn et al., 2019; Rodríguez-López et al., 2022). For example, Jiang et al. (2024), used SSD data from a long-term program monitoring water clarity dynamics in the Pearl River Estuary to regionalize WQP using the Landsat series and found improved water quality due to decreased anthropogenic perturbations and landscape change. Similarly, Caballero et al. (2022) proposed an innovative method to derive turbidity and Chl-a using S2 in a hypersaline coastal lagoon in the Western Mediterranean Sea and developed an early warning tool to monitor eutrophication processes with a high spatial resolution (10 m). In a more recent study, Zhang et al. (2024) employed S2 images to investigate spatiotemporal fluctuations in turbidity between 2016 and 2022 in an inland lake and examined the drivers of changes. Together, high-resolution S2 images for the visible and near-infrared bands, their frequent updates, and its neural network automated cloud detection system provide a valuable scientific resource for the study and monitoring of WQP (Alvado et al., 2021; Caballero et al., 2018; Caballero et al., 2020; Ciancia et al., 2020; Delegido et al., 2019; Pahlevan et al., 2017; Soomets et al., 2020; Sòria-Perpinyà et al., 2021; Sòria-Perpinyà et al., 2022; Zhan et al., 2022).

Different algorithms can be used to assess WQP. Lee et al. (2002), Nechad et al. (2009, 2010), Phuoc Hoang Son et al. (2013), Dogliotti et al. (2015), Balasubramanian et al. (2020), and Magrì et al. (2023) have contributed with valuable insights for the development of empirical and semi-empirical algorithms derived from satellite imagery. For example, Nechad et al., 2010, proposed an algorithm to estimate the concentration of suspended particulate matter (SPM) in Belgian coastal waters. The algorithm was tested and validated using *in situ* measurements, demonstrating a high degree of agreement between the satellite-derived SPM concentrations and the *in situ* measurements. In addition, the development of algorithms for atmospheric correction (AC) has facilitated the precise retrieval of turbidity in a variety of aquatic ecosystems. The combination of S2 images with new AC algorithms, such as ACOLITE, has enabled the exploration of WQP with high spatial resolution and low error (Caballero et al., 2020, 2022; Chowdhury et al., 2023; Jiang et al., 2024; Vanhellemont and Ruddick, 2016, 2018, 2021; Vijay Prakash et al., 2021).

The Northern Patagonia (NP) coastal region (41–45°S) is characterized by a complex geomorphology and high spatiotemporal variability

in hydrometeorological conditions. A combination of natural and anthropogenic forcings, for example, surface runoff and erosion of active forestry or agricultural areas following extreme precipitation events, are likely to contribute to turbidity in coastal waters (Curra-Sánchez et al., 2022; Iriarte et al., 2017; Lara et al., 2010; Lara et al., 2016; León-Muñoz et al., 2021; Saldías et al., 2019). On the other hand, the aquaculture of mytilids and salmonids, the main anthropic activity in the coastal areas of NP, has experienced enormous growth in recent years. According to FAO (2022), Chile is among the top ten producers of mytilid mussels and salmonids worldwide. In particular, the Reloncaví sound and fjord, at the equatorward edge of NP stand out for the intensive use of its coastal waters by aquaculture facilities, which also has altered WQP in the area (Astorga et al., 2018; Barria et al., 2012; Camelo-Guarín et al., 2021; Molinet et al., 2015, 2021). Earlier research around NP has provided some insights on the estimation and retrieval of WQP using remote sensing (Iriarte et al., 2017; Saldías et al., 2021; Vásquez et al., 2021). For example, Iriarte et al. (2017) used L3 MODIS-Aqua (Moderate Resolution Imaging Spectroradiometer) data to characterize spatial and temporal variability in Chl-a. Similarly, Saldías et al. (2021) and Vásquez et al. (2021) reported a peak of Chl-a and normalized Fluorescence Line Height (nFLH) during the austral autumn using MODIS-Aqua data with a resolution of 1 km. The spatial resolution of MODIS, however, is not sufficient to understand dynamic environmental processes, such as fluvial plume dispersion in the coastal ocean or WQP in small coastal and inland ecosystems. The potential of using the Nechad algorithms based on S2 images to understand turbidity, and more generally, the dynamics of WQP in NP remains largely unexplored, despite the importance of marine ecosystem health for human well-being in the region (Camelo-Guarín et al., 2021). To this end, we hypothesized that turbid waters in the Reloncaví area are primarily associated with seasonal processes, such as river discharge patterns. To tackle this hypothesis, we take advantage of S2 imagery, and examine the performance of the default algorithms, and test the accuracy of turbidity retrievals in time using *in situ* data available from an oceanographic buoy moored in the Reloncaví sound, and relate spatial patterns of turbidity to freshwater inflows using discharge data from a gauge of the main river drainage to the fjord.

2. Materials and methods

For a more comprehensive understanding, Fig. 1 illustrates the general methodological workflow diagram of this research. The sections depicted in Fig. 1 will be elucidated in greater detail below.

2.1. Study area

The Reloncaví sound located in Inner Sea Chiloé (ISC), Northern Patagonia, is a semi-enclosed basin of about 50 km in length (north-south) and a width of approximately 32 km (east-west), with depths that can reach 450 m. It is connected to the Pacific Ocean through the Chacao channel on the west (Fig. 2, GEBCO Gridded Bathymetry Data (GEBCO, 2024); Pinilla Matamala, 2011; Valle-Levinson et al., 2007). The climate is temperate maritime with annual rainfall between 3000 and 4000 mm per year, and temperatures range between 7 and 10 °C in winter, and 12 and 15 °C in summer (Aguayo et al., 2019; Garreaud, 2018; Garreaud et al., 2013; Lara et al., 2018; Subiabre and Rojas, 1994). Weather can be highly variable, driving quick changes in sea surface temperature (SST) driven by strong southerly winds. Harmful algal blooms (HABs) are common (Díaz and Figueroa, 2023; Saldías et al., 2021; Sandoval et al., 2018; Soto-Mardones et al., 2009). Water circulation in the fjord and sound is influenced by tides, currents, and winds (Pantoja et al., 2011; Pérez-Santos et al., 2019; Pérez-Santos et al., 2021; Vásquez et al., 2021). The sound receives large freshwater discharges from the Reloncaví fjord, the drainage of the Puelo, Petrohué, and Cochamó rivers.

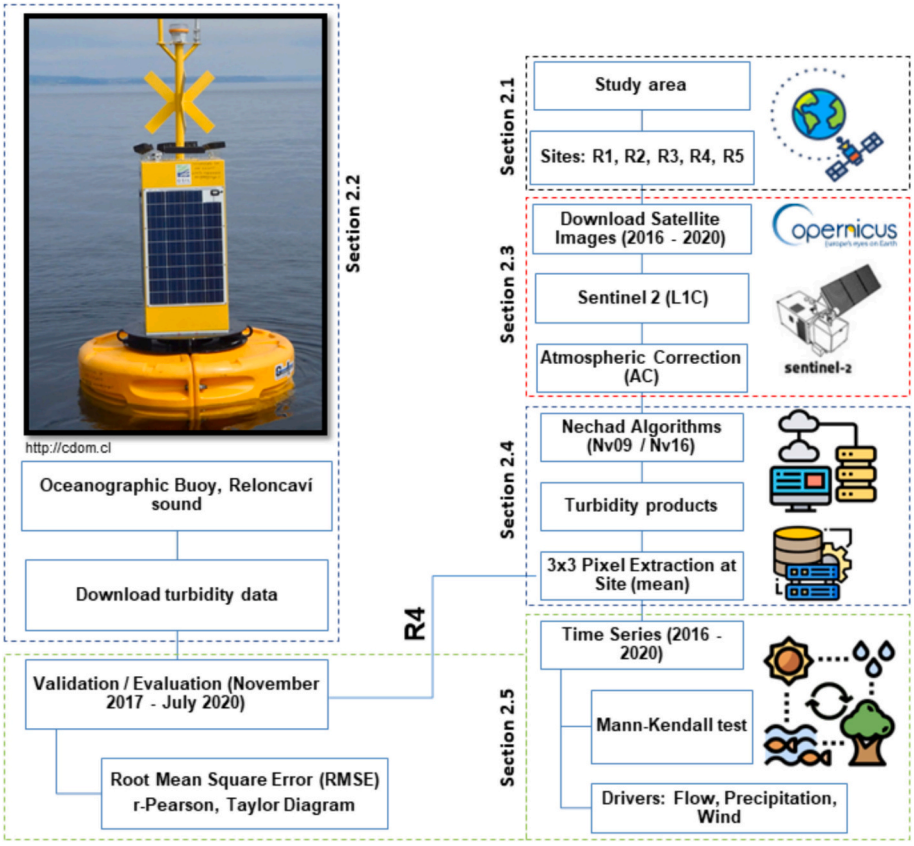

Fig. 1. Methodological workflow diagram.

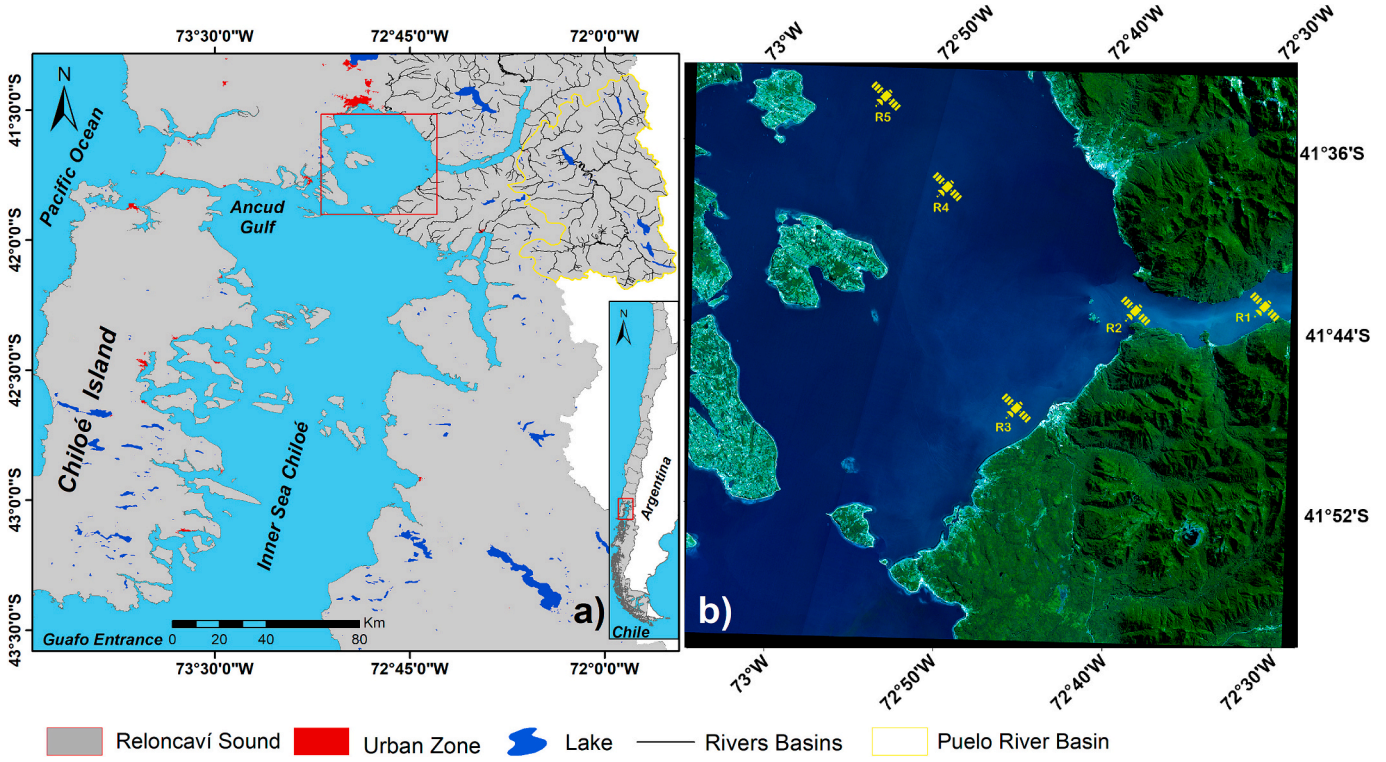

Fig. 2. (a) Location of the study area in Northern Patagonia. The red box indicates the Reloncaví sound area. Urbanized areas are indicated in red, freshwater lakes in blue, rivers draining into the study basins are shown in black lines, and the Puelo river basin is in yellow line. (b) RGB (True color) image of the area enclosed in the red box in (a) showing the spatial distribution of the sampling sites (R) in the Reloncaví sound and fjord, which are distributed from inside the fjord (R1), at the fjord mouth (R2), the fjord plume (R3), next to the oceanographic buoy (R4) and away from the influence of riverine discharges (R5). (For interpretation of the references to color in this figure legend, the reader is referred to the web version of this article.)

These Andean rivers exhibit a pluvio-nival regime, resulting in large outflows of suspended and dissolved material into the coastal zone (Aguayo et al., 2019; Iriarte et al., 2014; León-Muñoz et al., 2013, 2021; Saldías et al., 2019). The Puelo river exhibits the third largest discharge of the southwestern Andes with an outflow of mean annual flows of approximately 670 m/s (Lara et al., 2008). On the other hand, the Reloncaví fjord is one of the main areas for the capture of wild mussel seed (larvae), which are used locally for mussel aquaculture, in addition to the salmon farms located there (Barria et al., 2012; Buschmann et al., 2009; Buschmann et al., 2021; Camelo-Guarín et al., 2021; Molinet et al., 2021).

2.2. *In situ turbidity, fluviometric, and meteorological datasets*

We used *in situ* turbidity data extracted for the period between November 2017 to July 2020 from a moored oceanographic buoy (OSIL's Fulmar) belonging to the i-mar Center of the Universidad de Los Lagos and Reloncaví Marine Observatory. The buoy is located in the Reloncaví sound at −41°38′10" S and − 72°50′4" W, adjacent to R4 (Fig. 2b). Turbidity is measured using a multiparameter probe (AML Metrec XL). To store the turbidity dataset, the instrument has an hourly GSM transmission system and an onboard datalogger. The extracted data were segmented to the mean of the values recorded between 14:00 and 15:00 h (local time), coinciding with the satellite visit time in the study area, with a time difference window of ±1 h. Turbidity data can be downloaded from the website http://www.cdom.cl/ (accessed May 2022). To study the spatial distribution of turbidity in the study area, we selected five sites, where we estimated turbidity over a 3 × 3 pixel window (90 m^2, see Fig. 2b). The location of sites was selected to span a range of conditions and were located inside the fjord and influenced by the river (R1), at the fjord mouth (R2), in the plume of the river inside the sound (R3), at the location of the oceanographic buoy in the sound (R4) and finally, on a location inside the sound and an away from the influence of the discharge of any major rivers (R5). To illustrate the role of local meteorological forcing on turbidity, a time series of daily river flow and daily precipitation measured at the Puelo river meteorological station are presented. Precipitation and river flow data were downloaded from the Dirección General de Aguas (DGA, https://dga.mop.gob.cl/, accessed November 2023). The wind (speed and direction) values were taken from https://climatologia.meteochile.gob.cl/ in a three-day window (72 h) before the image acquisitions.

2.3. *Remote sensing images and processing*

Cloud cover (CC) is common in our study area. Hence, we conducted a detailed visual inspection of each of the images in the date range of our study. The image selection process yielded a dataset with a minimum

Table 1
Number of selected Sentinel-2 images for the 2016–2020 period.

Month / Year	2016	2017	2018	2019	2020	Total
January	1	1	3	2	6	13
February	1	1	3	3	2	10
March	0	2	2	5	2	11
April	0	2	3	1	2	8
May	0	1	2	2	4	9
June	1	0	2	3	1	7
July	2	2	2	0	2	8
August	0	1	2	0	3	6
September	1	2	1	3	2	9
October	1	2	2	5	5	15
November	1	1	4	3	2	11
December	3	2	4	3	4	16
Total	11	17	30	30	35	123

0: No images available or No clear.

and maximum CC of 0 % and 57.9 %, respectively for the full scene. We analyzed a total of 123 images from 2016 to 2020 (see Table 1). Further details are provided in Supplementary Material 2 (SM 2).

The S2 mission is based on a constellation of two identical satellites (2A/2B) in the same orbit, 180° out of phase with each other. Each satellite carries one MSI (Multispectral Instrument) sensor, with a revisit frequency of five days at latitudes near the equator, and higher frequencies at higher latitudes due to orbital overlap, (2 to 3 days for the study area) and with a radiometric resolution of 12 bits. Table 2 shows the spectral and spatial resolution of S2 (ESA - European Space Agency, 2015). The S2 images are provided at two processing levels: Level 1C (L1C), which are radiometrically and geometrically corrected to the Top Of Atmosphere (TOA), and Level-2A (L2A) which provides atmospherically corrected surface reflectance images, derived from the associated Level-1C products. The AC of S2 images includes the correction of the scattering by of air molecules (Rayleigh scattering), of the absorbing and scattering effects of atmospheric gasses, in particular ozone, oxygen, and water vapor, and the correction of absorption and scattering due to aerosol particles (ESA - European Space Agency, 2015). For this work, a total of 123 S2-L1C scenes over the study area were free-downloaded from the Sentinel Science Data Center (https://dataspace.copernicus.eu, accessed May 2022).

Using ACOLITE (free software, https://github.com/acolite/), we applied AC to the S2 images to go from the L1C processing level to the L2A processing level. ACOLITE is a generic algorithm developed at Royal Belgian Institute of Natural Sciences (RBINS) for atmospheric correction and processing of satellite imagery for coastal and inland waters, allowing the correct estimation/validation of the turbidity parameter (Vanhellemont, 2019, 2020; Vanhellemont and Ruddick, 2018), supporting different types of multispectral and hyperspectral sensors, including S2 (Vanhellemont and Ruddick, 2016). We used the default DSF "Dark Spectrum Fitting" method of the software (Vanhellemont, 2019, 2020; Vanhellemont and Ruddick, 2018). All S2 images (L1C level) were atmospherically corrected with ACOLITE (version 20221114); output data correspond to water reflectance at a wavelength (λ)($\rho_w(\lambda)$), resampled to a pixel size of 10 m. $\rho_w(\lambda)$ is defined in Eq. (1):

$$\rho_w(\lambda) = \pi L_w(\lambda) / E_d^{0+}(\lambda) \quad (1)$$

where $L_w(\lambda)$ represents the water-leaving radiance (after removal of air-water interface reflection) and $E_d^{0+}(\lambda)$ is the downwelling irradiance.

In addition, a built-in algorithm in ACOLITE optionally performs sunglint contamination corrections on SWIR band sensors (Harmel et al., 2018; Vanhellemont, 2019). We selected this sunglint correction to obtain the reflectance of the glint-free surface.

Table 2
Spectral and spatial resolution of S2.

Bands	Spectral region	Spatial resolution (m)	λ_{S2A} (nm)	λ_{S2B} (nm)	Bandwidth $_{S2A}$ - $_{S2B}$ (nm)
B1	Coastal aerosol	60	442.7	442.2	21–21
B2	Blue	10	492.4	492.1	66–66
B3	Green	10	559.8	559	36–36
B4	Red	10	664.6	664.9	31–31
B5	Red-edge1	20	704.1	703.8	15–16
B6	Red-edge2	20	740.5	739.1	15–15
B7	Red-edge3	20	782.8	779.7	20–20
B8	NIR	10	832.8	832.9	106–106
B8A	NIR narrow	20	864.7	864	21–22
B9	Water vapor	60	945.1	943.2	20–21
B10	SWIR / Cirrus	60	1373.5	1376.9	31–30
B11	SWIR1	20	1613.7	1610.4	91–94
B12	SWIR2	20	2202.4	2185.7	175–185

2.4. Turbidity algorithms

ACOLITE incorporates two functions to estimate turbidity based on Nechad's algorithms (Nechad et al., 2009, 2016), hence we used both to estimate turbidity for all sites and dates (2009, Nv09, and 2016, Nv16, respectively). The Nv16 algorithm version was recalibrated in 2016 by Bouchra Nechad using the Nv09 algorithm, specifically for S2 and L8 (Nechad et al., 2016). In Nechad's approach, turbidity is derived using a semi-empirical algorithm relating spectral reflectance to IOPs absorption and backscatter:

$$\text{Turbidity} = \frac{A_T\,\rho_w(\lambda)}{1-\rho_w(\lambda)/C} + B_T \quad (2)$$

where A_T, B_T and C are wavelength-dependent calibration coefficients encompassing IOPs characteristics (for more details see Nechad et al., 2009, 2010, 2016). We employ the red band (λ = 665 nm), which is related to S2 band 4 (B4) of S2 (see Table 2).

The oceanographic buoy located at R4 provides *in situ* turbidity data in NTU units, yet for practical purposes we present the data in FNU units for comparison with turbidity from Nechad's algorithms (Anderson, 2005; Dogliotti et al., 2015). The mean turbidity value was extracted in a 3 × 3 pixel kernel centered on the *in situ* measurement location, which we used to construct a time series for the 2016–2020 period. Following guidelines by Huettmann and Arhonditsis (2023), all data is available from the Zenodo repository (https://zenodo.org/doi/10.5281/zenodo.13645864).

2.5. Statistical analysis

Firstly, we carried out an exploratory analysis with all the *in situ* (buoy) turbidity data to detect outliers using descriptive statistics. To remove possible outliers in the *in situ* and satellite data we used a 25 % deviation of the standard deviation (SD) criteria. For the *in situ* data, we examined turbidity measurements during the satellite overpass, and for the satellite data we used the data in each 3 × 3 pixels spatial window. The resulting *in situ* observations were match-up with the data from the images available for the turbidity product. A total of 39 satellite images were used for the match-up exercise of satellite data with the data from the buoy located at the R4 site. Then, we compared *in situ* turbidity and the Nv09 and Nv16 algorithms using linear regression and quantified the agreement using the coefficient of determination (R^2), Pearson's correlation (Pearson's r), root-mean-square-error (RMSE), centered root-mean-square-error (CRMSE) difference, and the amplitude of their variations represented by their SD, which were visualized using a Taylor's diagram (Taylor, 2001). To compile the satellite time series for each site we included the 123 valid images (Table 1). However, following the sparse and uneven sampling of turbidity data in time we used simple exponential smoothing from the Simple Time Series Analysis app from OriginPro (Academic version 2023b 10.0.5.157) software to visualize patterns and trends in time. Similarly, we used a Mann-Kendall (MK) test to evaluate turbidity trends at all sites. Finally, we analyzed a time series of records of precipitation and river flow data together with our turbidity values derived from the Nv09 algorithm at R1, the more landward station. The reconstructed time series from R1 to R5 allowed us to discern the presence of seasonal patterns of turbidity in our study area and examine the role of precipitation and river flow on turbidity in the Reloncaví coastal ecosystem. To this end, we wanted to test the hypothesis that using the Nechad algorithms we could (a) detect seasonal patterns in the presence of turbid waters across the fjord-sound waters and that (b) the presence of turbid waters was associated with large riverine outflow events.

3. Results

3.1. In situ turbidity

Table 3 shows the statistics for *in situ* turbidity records during the 2017–2020 period. The turbidity values ranged from 0.18 FNU to 7.57 FNU across the year. The minimum value was recorded during austral spring (0.18 FNU), while the maximum was found in austral autumn. The mean of the 39 match-up values for *in situ* comparisons was 1.94 FNU. The large variation across turbidity match-up values is underlined by the CV (Table 3.)

3.2. Turbidity algorithms

Fig. 3a shows the relation between the two algorithms (Nv09 and Nv16) and the *in situ* turbidity measurements (site R4). The linear relationship with *in situ* data for both algorithms was nearly identical ($R^2 = 0.40$, Pearson's $r = 0.63$, Fig. 3a). However, the Nv09 algorithm presented a lower RMSE than the Nv16 algorithm (see Fig. 3a). A similar result was observed in the Taylor analysis (Fig. 3b). The Nv09 and Nv16 algorithms reported a Pearson's r = 0.63 (matching with the linear fit), and Nv09 presented lower variability among its data (SD = 0.83 FNU), with CRMSE less than 1.34 FNU. Therefore, it is possible to suggest that both algorithms have a good correlation with *in situ* turbidity. Nevertheless, the Nv09 algorithm appears to be the most reliable option for developing a turbidity predictor model in the study area at wavelengths of 665 nm, which is supported by the lower CRMSE and SD (Fig. 3b).

Fig. 4 shows true color (RGB) images derived from S2 images (top panel) and turbidity maps from the Nv09 algorithm (bottom panel) for austral autumn. The turbidity maps are presented in logarithmic scale following the high turbidity level observed during austral autumn. Using the Nv09 algorithm the highest estimated value was greater than $\log_{10}$ 1.29 FNU for 2019-May-06 and 2020-May-20. It is important to note that the highest turbidity values observed in austral autumn correspond to large freshwater outflows from the Puelo river (see Fig. 4).

3.3. Spatio-temporal analysis

The use of both algorithms in all sites captured the same temporal pattern when estimating high and low turbidity values at all sites (see SM1 Figs. 1, 2, 3) and hereafter we present results only for the Nv09 algorithm. More information on the estimated turbidity values by both algorithms can be obtained from SM1.

During the austral summer, the values ranged from 0.3 FNU to 5 FNU, with R5 and R1 sites recording the lowest and highest values, respectively (see Fig. 5, SM1 Fig. 4). Temporal patterns of turbidity were stable among study sites with CV between 24 % and 37 %. Sites R1 to R4 had a CV of less than 30 % and only site R5 exceeded this figure (see SM1 Table 3 and SM1 Fig. 5a). In space, stations closer to the river showed higher turbidity values; in time the highest values are observed during autumn and the lowest in spring (see Fig. 5).

Fig. 6 shows that the lowest turbidity value was 0.090 FNU at site R5 (see SM1 Table 2). The austral springs were characterized by the lowest turbidity values, minimum values less than 1 FNU were detected at sites R3 to R5 (see Figs. 5, 6). The highest turbidity values during spring were obtained at sites R1 and R2, both exceeding 7 FNU and 4 FNU, respectively (see SM1 Fig. 5d). Turbidity in sites R1 and R2 showed low variability compared to site R5, where CVs ranged from 31 % to 57 % during this season (see SM1 Table 6). On the contrary, high turbidity values were found in autumn, specifically in May (see Fig. 5, and SM1 Fig. 4). Over the time series, the highest estimated turbidity value was 27.962 FNU in the autumn of 2019 at site R1 (see Figs. 5, 6, and SM1 Table 2). In this same season, one year later, high turbidity values were observed in all sites (see Fig. 5). In the autumn of 2020, sites R2, R3, and R4 reached their maximum turbidity with values of 19.556 FNU, 8.721 FNU, and 5.285 FNU respectively (see Figs. 4, 5, 6, and SM1 Fig. 5b). The largest turbidity variations were observed at sites R1 and R2 in the autumn, and the smallest at site R5 (see SM1 Table 4). Little variation in turbidity among all study sites was recorded in winter with CVs ranging between 24 % and 35 %, similar to the behavior found in the summer, maximum values remained between 3 FNU and 4 FNU for all study sites (see Fig. 6, and SM1 Fig. 5c). The largest variation in turbidity was recorded at site R5 and the lowest at site R2, opposite to what we recorded in autumn (see SM1 Table 5). We observed no significant temporal trends in all the reconstructed time series. Although exponential smoothing and the MK test showed a slight increase in turbidity at sites R1 and R2 during the study period, this was not observed at sites R3, R4, and R5 (see Fig. 6, and SM1 Table 1).

Table 3
Descriptive statistics of *in situ* turbidity measured during the period 2017–2020.

Statistical / Season	Summer	Autumn	Winter	Spring	Total
min (FNU)	0.31	2.05	0.5	0.18	0.18
max (FNU)	5.04	7.57	3.48	2.75	7.57
mean (FNU)	1.89	4.3	1.68	1.08	1.94
SD	1.59	2.08	1.09	0.87	1.72
CV (%)	84.04	48.34	64.87	80.87	88.84
n	14	6	5	14	39

min/max— minimum/maximum turbidity values, SD—standard deviation, CV—coefficient of variation, and n—data number.

4. Discussion

Worldwide, turbidity has been estimated for aquatic ecosystems through remote sensing using spectral band ratios and algorithms. To this end, the Nechad algorithms have been applied to multiple inland and coastal ecosystems around the world due to their accuracy in deriving high and low turbidity values as in Nechad et al. (2009, 2010, 2016), Dogliotti et al. (2015), Novoa et al. (2017) and Tavora et al. (2023a). However, studies related to spatial and temporal turbidity variability in coastal marine ecosystems are still scarce (Caballero et al., 2022; Chowdhury et al., 2023; Jiang et al., 2024,). Our study represents the first time that the ACOLITE turbidity algorithms have been used and validated on the NP marine ecosystem, which we extended to the examination of the spatial and temporal dynamics of a turbid river.

Advances in algorithms for AC have allowed the accurate retrieval of WQP. The studies summarized in Table 4 demonstrate the effectiveness of ACs for the study of turbidity in aquatic ecosystems. Elhag et al. (2019) applied the NDTI index (Normalized Difference Turbidity Index), derived from Sentinel 2 Correction (Sen2Cor), and obtained R^2 values between 0.74 and 0.94. Delegido et al. (2019) combined *in situ* measurements of SDD with band ratios using different ACs, obtaining medium to high R^2 (0.34–0.82) and low RMSE (1.4 NTU and 2.7 NTU). Meanwhile, Zhan et al. (2022) applied similar techniques to estimate turbidity in a hypersaline coastal lagoon, obtaining a similar R^2 and error variation. Nevertheless, it is important to note that the errors observed in our study were among the lowest presented in Table 4.

The versatility of ACOLITE distinguishes it from other AC. ACOLITE enables the processing of images from a variety of satellite missions, which have contributed to the management and monitoring of aquatic ecosystems over time (Caballero et al., 2020, 2022; Jiang et al., 2024; Kuhn et al., 2019; Novoa et al., 2017; Paulista et al., 2023; Rodríguez-Benito et al., 2020; Rodríguez-López et al., 2022; Tavora et al., 2023b; Vijay Prakash et al., 2021). For example, Sun et al. (2021) and Chowdhury et al. (2023) estimated turbidity using ACOLITE with S2 and obtained $R^2 = 0.67$ and $r = 0.97$, respectively. Consistent with the aforementioned studies, our R^2 value was found to be within the ranges reported in Table 4. This can be attributed to the multiple processes that take place across our study area, such as algal blooms, strong winds, precipitation, and discharge from multiple streams and rivers. In addition, the quality and quantity of CDOM and SS associated with river discharge (Curra-Sánchez et al., 2022, 2024; Davies-Colley and Smith,

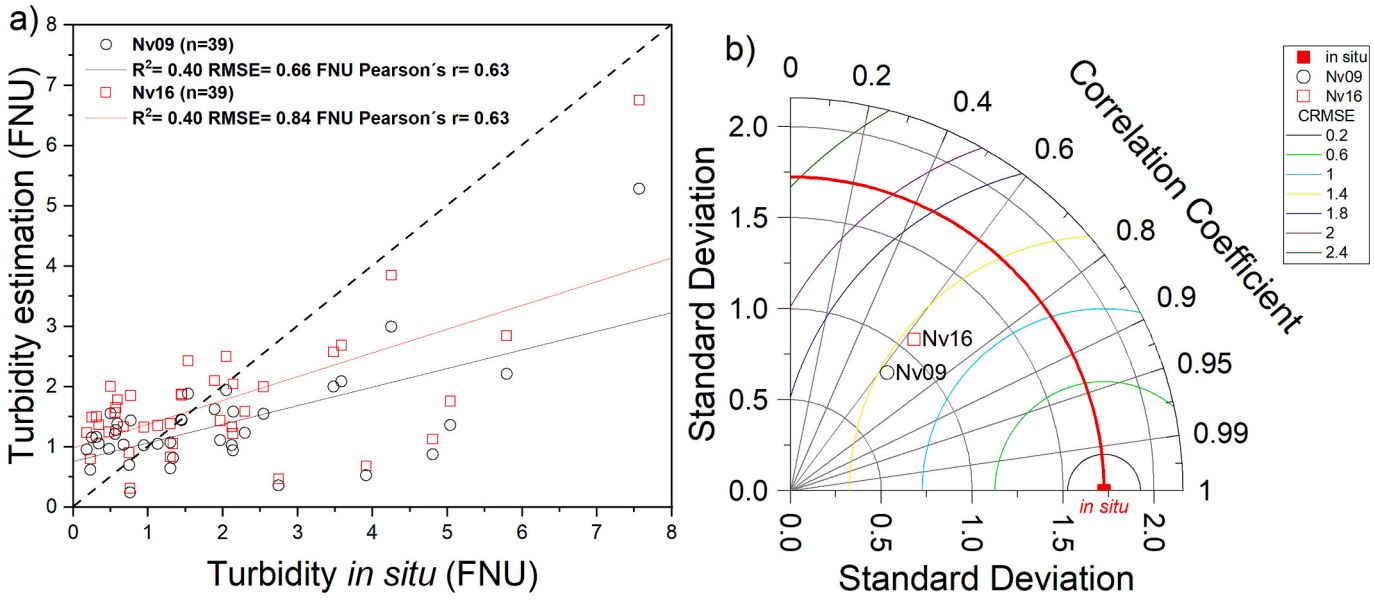

Fig. 3. (a) Scatter plot between measured turbidity and the algorithms under study. The black circle and line represent the values from the Nechad 2009 algorithm (Nv09), while the red square and line are those resulting from the Nechad 2016 algorithm (Nv16), dash line represents a 1:1 line. (b) Taylor diagram displaying a simultaneous statistical comparison of both algorithms and *in situ* turbidity measurement. The colored contours indicate the CRMSE values. (For interpretation of the references to color in this figure legend, the reader is referred to the web version of this article.)

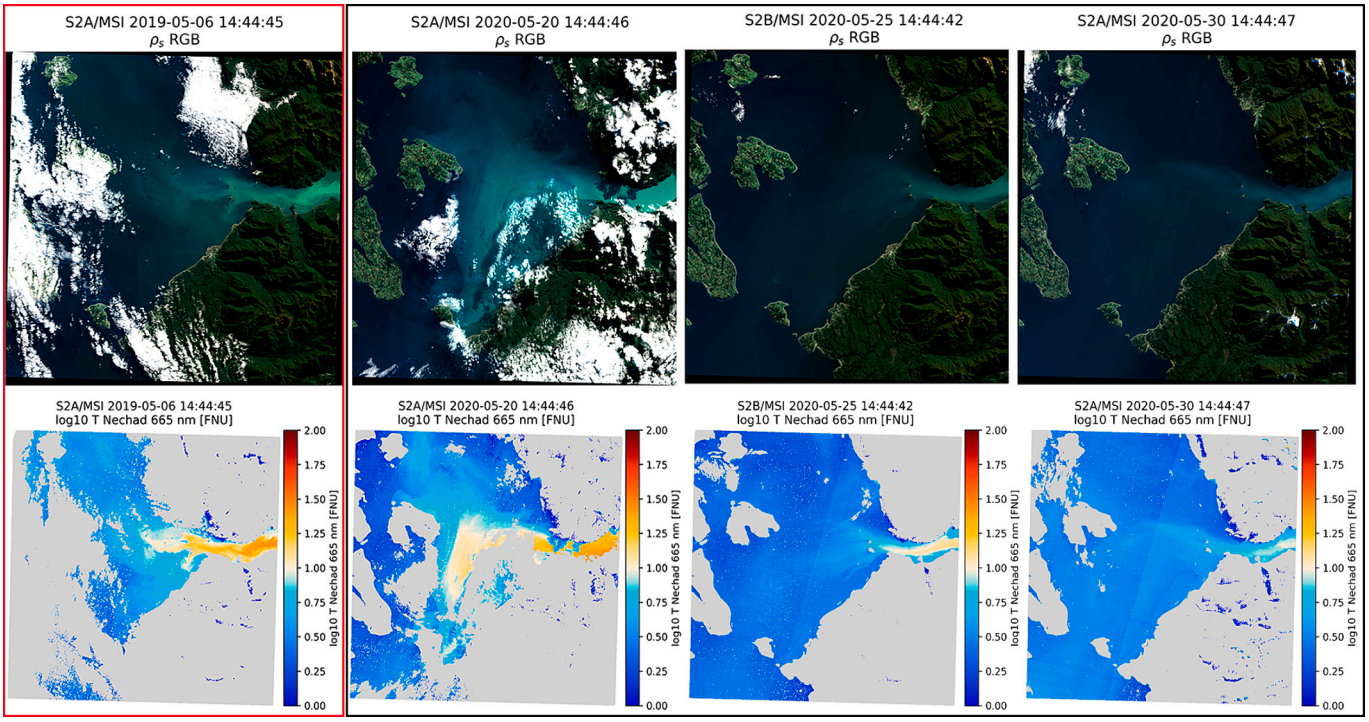

Fig. 4. The top panels show true color (RGB) images and the bottom panels show results from the Nv09 algorithm for the autumn days where we detected high turbidity. The top and bottom far left panels (red panel) show the image with the highest turbidity on May 6th, 2019. All images show the turbid plume streaming out of the fjord into the sound. (For interpretation of the references to color in this figure legend, the reader is referred to the web version of this article.)

2001; Vijay Prakash et al., 2021) in the area, are linked to both pluvial or nival regimes (Garreaud et al., 2013; León-Muñoz et al., 2013, 2021), which results in fluctuations in water clarity and quality. The ACOLITE turbidity algorithms proved effective to estimate turbidity in the NP marine ecosystem. Is important to note that the algorithm's performance can vary depending on the characteristics of the study area. In highly turbid waters (case II waters) or during extreme events, some algorithms may produce higher errors, as demonstrated by Chowdhury et al. (2023), which highlights the need for continual assessment of algorithm performance for the effective monitoring and management of these important environments.

Future studies may wish to implement other ACs or other variants/techniques beyond ACOLITE for turbidity derivation and integration of time series using satellites such as L8. A method proposed by Zhang et al. (2024) employed machine learning models to estimate turbidity using NDTI and band ratio accurately. However, it is important to consider

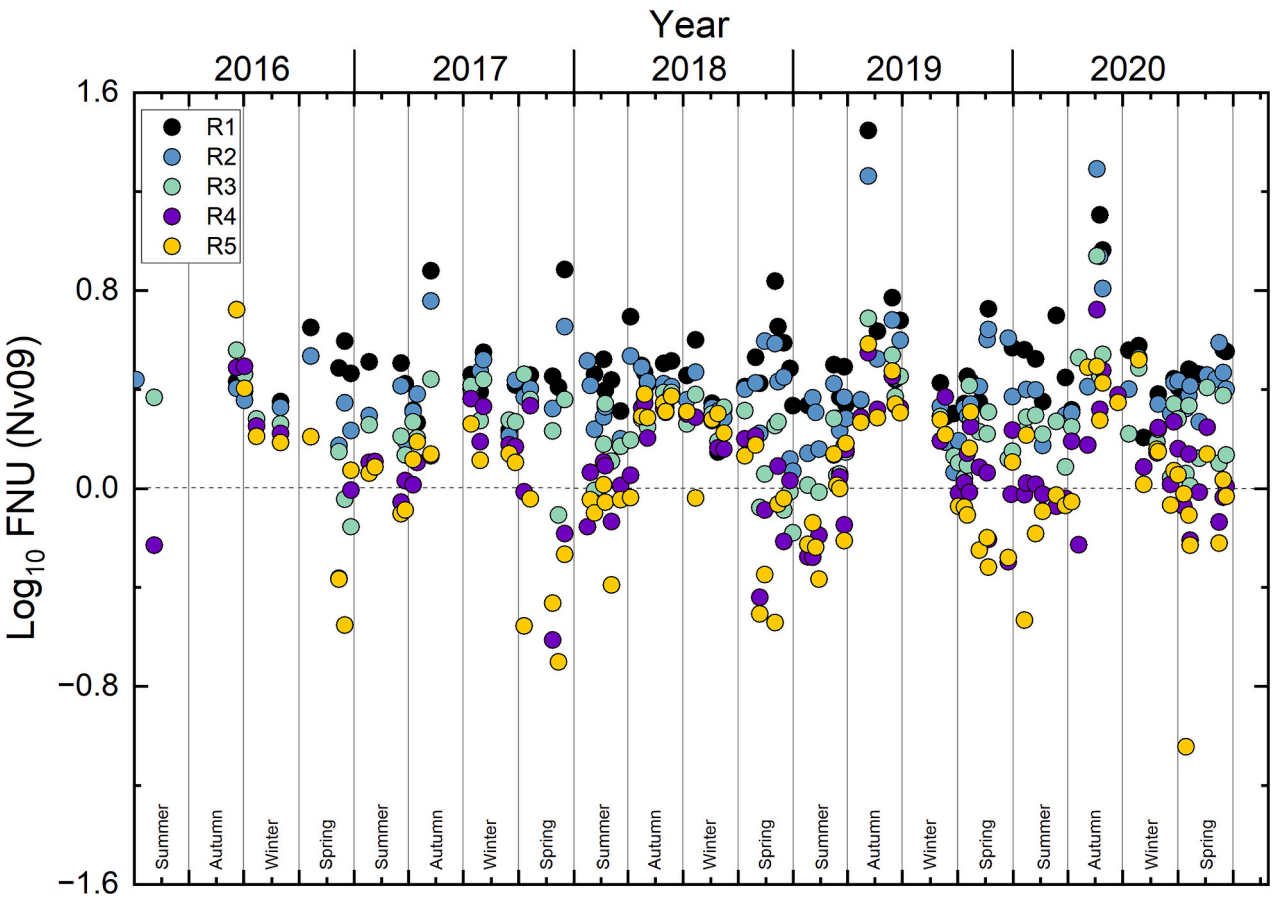

Fig. 5. Spatio-temporal distribution of turbidity derived from the Nv09 algorithm for all sites. The sites are identified by the following color codes: R1 in black, R2 in light blue, R3 in light green, R4 in purple, and R5 in mustard. (For interpretation of the references to color in this figure legend, the reader is referred to the web version of this article.)

that the results may have been influenced by the type of ecosystem examined, a eutrophic lake, by the presence of aquatic vegetation, and the high Chl-a concentration. On the other hand, Lizcano-Sandoval et al. (2022) applied the same index (NDTI) to S2 imagery in west-central Florida and used turbidity to exclude images before mapping temporal changes in submerged seagrass. The evaluation and comparison of turbidity behavior in the spectral region of the Red-edge and near-infrared (NIR) be considered (see Table 2). Chowdhury et al. (2023) demonstrate that water turbidity is sensitive to different wavelengths within this spectral range. In this sense, in future studies, it would be advisable to test both algorithms (Nv09 and Nv16) at different wavelengths. This is to detect and determine how the turbidity values behave in the Reloncaví sound in different spectral ranges. The Nv16 algorithm may obtain better results when tested at wavelengths longer than 665 nm.

Remote sensing applications for aquaculture are promising tools for managing the challenges of ongoing climatic change (Newell et al., 2021; Snyder et al., 2017). Mussel aquaculture in NP is under challenges that threaten to disrupt current patterns of climatic and environmental variability, including the seasonal dynamics of environmental factors such as Chl-a, SS, CDOM, HABs, salinity, SST, pH, dissolved oxygen (DO), winds, turbidity, among others (Castillo et al., 2016; Curra-Sánchez et al., 2022; Iriarte et al., 2007; Iriarte et al., 2017; Lara et al., 2016; León-Muñoz et al., 2018; Molinet et al., 2015; Pantoja et al., 2011; Soto et al., 2019). Seasonal patterns in turbidity are evident, with maximum values during austral autumn for all years of our study period in association with changes in mean precipitation (*e.g.*, autumn 2017, 2019, and 2020). Precipitation directly influences the outflow of water into the sound from the Puelo river, as reported by Aguayo et al. (2019) and León-Muñoz et al. (2013, 2021). The linkage between precipitation and large turbid plumes entering the Reloncaví sound was apparent in our study (see Figs. 4, 7), and the results of Flores et al. (2022) support this behavior/pattern. Similar results were reported by Shen et al. (2021) and Mahmoud et al. (2023), in Asia, who showed that turbidity at the confluence of river tributaries or the highest concentrations of SS, Chl-a, and dissolved solids, respectively, were associated with heavy rainfall.

The greatest extent of turbid plumes took place in the autumn of 2019 and 2020, following the most severe storms of the year and the highest turbidity value at site R1 (27.96 FNU derived from the Nv09 algorithm). The highest turbidity values appear coincident with the most pronounced discharge events occurring during 2019-May-02, 2020-May-16, and 2020-May-25 (Fig. 7). Conversely, less rainy seasons and curtailed river discharge are often associated with less conspicuous plumes and low turbidity values (*e.g.*, summer 2018). Therefore, in agreement with our hypotheses, the variation of maximum turbidity values seems to be influenced by the combination of precipitation and fluvial discharge from the river, especially in autumn and thus follows a seasonal pattern. This results in a discernible seasonal pattern.

Iriarte et al. (2017) reported changes in phytoplankton concentrations associated with intra-annual variability in the hydrological regime of the Puelo river during 2003–2011. Higher concentrations of Chl-a and phytoplankton abundance in surface waters were observed when flows were lower than 350 m^3s^{-1}, coinciding with dry austral autumns during the El Niño event (*e.g.* January–June 2007). This resulted in a decoupling between outflows and Chl-a in surface waters. Similar results were found by Saldías et al. (2021) for the study area in the ISC seasonal

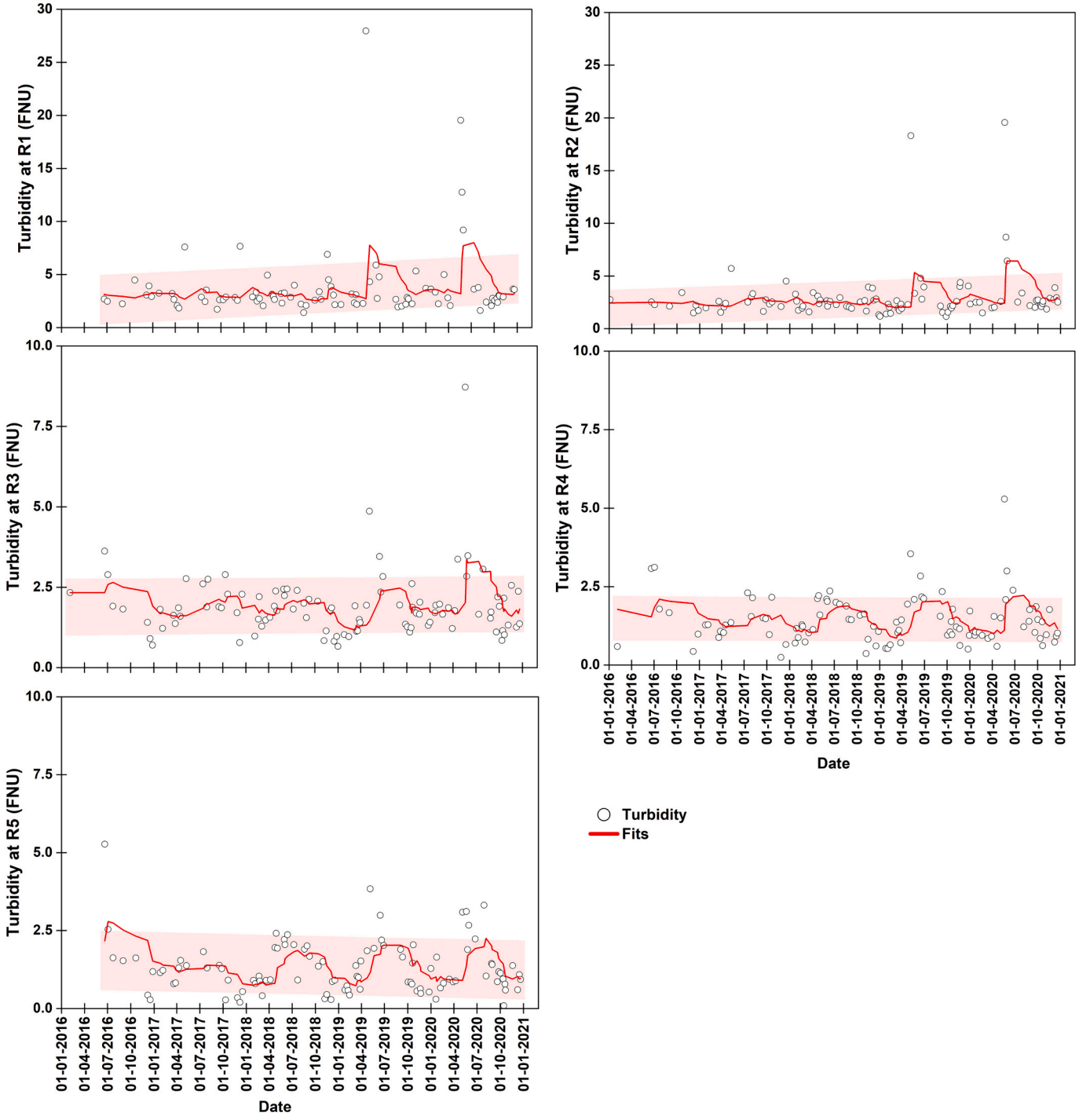

Fig. 6. Turbidity time series constructed for all sites for the period 2016–2020. Black circles show the estimated turbidity time series from the Nv09 algorithm, and the red line represents the smoothing fit with a 95 % prediction band (confidence interval). (For interpretation of the references to color in this figure legend, the reader is referred to the web version of this article.)

climatology (2003–2019), reporting the maximum values of nFLH in the austral autumn. Likewise, Vásquez et al. (2021) reported elevated Chl-a and nFLH peaks during April, May and June. These peaks in Chl-a may have been influenced by periods of high river discharge, together with other factors such as wind, SST fronts, or changes in the physical structure of the water column. The growth of phytoplankton can be facilitated by river discharges in the presence of nutrients and other oceanographic variables (Paudel et al., 2016). In a recent study, Mahmoud et al. (2023) demonstrated a correlation between water temperature and Chl-a, a relationship that is also influenced by sunlight, which directly affects phytoplankton growth. On the other hand, Zhang et al. (2024), using a machine learning approach, found a strong and positive correlation between turbidity and Chl-a concentration, indicating that changes in Chl-a can modulate variations in turbidity. These studies indicate that the high Chl-a in the austral autumn could be coincident with the elevated water turbidity found in this study (see Figs. 5, 7, and SM1 Fig. 4, 5b). Our findings demonstrated a direct relationship between large precipitation events leading to high river streamflow, and increased turbidity (see Figs. 3, 5, 7). Hence, high Chl-a values in MODIS Chl-a in our study system may follow from the presence of SS and CDOM

Table 4
Comparison between different satellite-based atmospheric correction (AC) algorithms to estimate turbidity in aquatic ecosystems, using several statistical indicators.

Authors	AC	R^2	RMSE	Aquatic Ecosystem	Location
Delegido et al. (2019)	C2RCC, C2X and Polymer	0.34–0.82	1.4 NTU and 2.7 NTU	Reservoirs	Valencian Community, Spain
Elhag et al. (2019)	Sen2Cor*	0.74–0.94	0.07–1.15 (NDTI)	Baysh Dam	Wadi Baysh, Saudi Arabia
Sun et al. (2021)	ACOLITE	0.62–0.77	3.13 NTU - 5.21 NTU	Lakes	Wuhan, China
Zhan et al. (2022)	C2X	0.64–0.73	1.5 NTU - 1.7 NTU	Hypersaline Coastal Lagoon	Mar Menor, Spain
Chowdhury et al. (2023)	ACOLITE	0.97 (r)	15.93 FNU	Guadalquivir Estuary	Gulf Cadiz, southern Spain
This study	**ACOLITE**	**0.40/0.63 (r)**	**0.66 FNU**	**Sound/Coastal Zone**	**Reloncaví sound, NP, Chile**

Atmospheric Correction (AC), determination coefficient (R^2), Pearson's correlation coefficient (r), Root Mean Square Error (RMSE).
* Is not indicated, only S2 satellite images are mentioned.

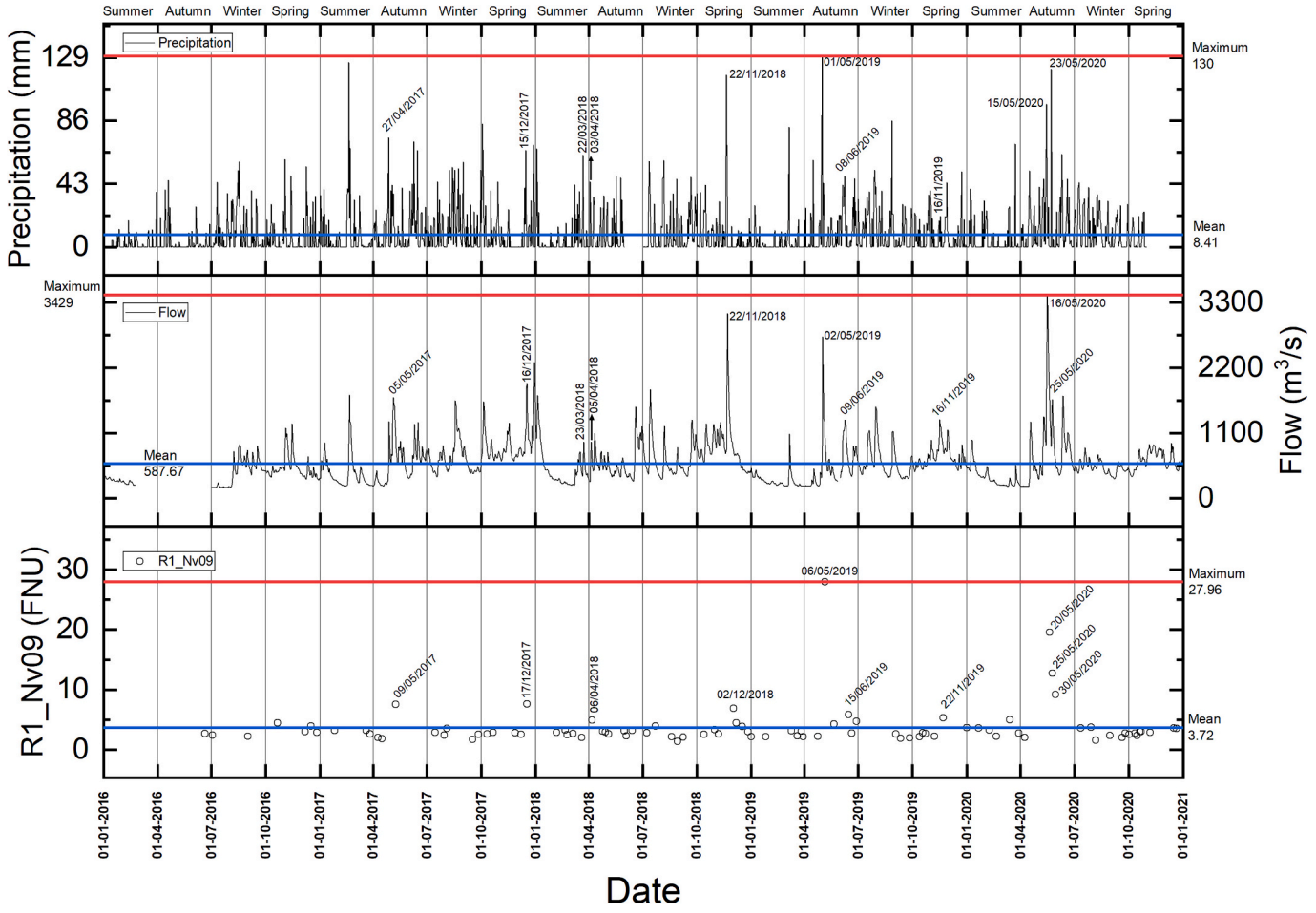

Fig. 7. Time series of precipitation and river flow data from DGA, and turbidity data at location R1 derived from the Nechad 2009 algorithm (Nv09).

from surface runoff from the adjacent basins during certain periods of the year.

The discharge and influence area of the river plume increases turbidity in the coastal zone. This study confirms that this turbidity behavior is maintained over time (see Figs. 4, 5, 7). The highest turbidity values were found in the fjord and fjord mouth (R1 and R2). In this sense, Curra-Sánchez et al. (2022) found that turbid waters in a river and estuary in the ISC were caused by high concentrations of CDOM from river discharge, mainly of allochthonous origin. Given the strong relationship between turbidity and total suspended matter (R^2 = 0.82), Chowdhury et al. (2023) showed that in-stream and estuarine sites had the highest turbidity values consistent with our results. Using hydrological models Aguayo et al. (2019) estimated future discharge scenarios of the Puelo river and found a trend of high discharge during May, June, and July (late austral autumn, and early austral winter), which was driven by abundant precipitation. We foresee that this scenario could lead to a river plume of high turbidity, as shown in our results. Our results show that as we move away from the river discharge, turbidity decreases, as was the case at sites R4 and R5 (see Fig. 5). However, on some occasions in austral autumn, both sites recorded values close to 5 FNU (see Figs. 5, 6, and SM1 Table 4). The high turbidity levels at these sites may be also driven by wind forcing of river plumes. Flores et al. (2022) used MODIS (λ = 645 nm) to detect the river plume in the Reloncaví sound and observed elevated reflectance values of this band. Hence, the B4 band (see Table 2) in the Nechad algorithm appears as an effective means of detecting the river plume and turbid waters.

Fig. 8 shows the wind compass 72 h before the acquisition of the four S2 images where we detected high turbidity. The first three dates provide evidence that the highest wind frequency (>30 %) corresponds to northerly wind with speeds above 4 kt (7.2 km/h), coincident with increasing turbidity in the seaward sites. Similar results have been reported by Banas et al. (2005), Hyun (2007), Abirhire et al. (2020), Soria

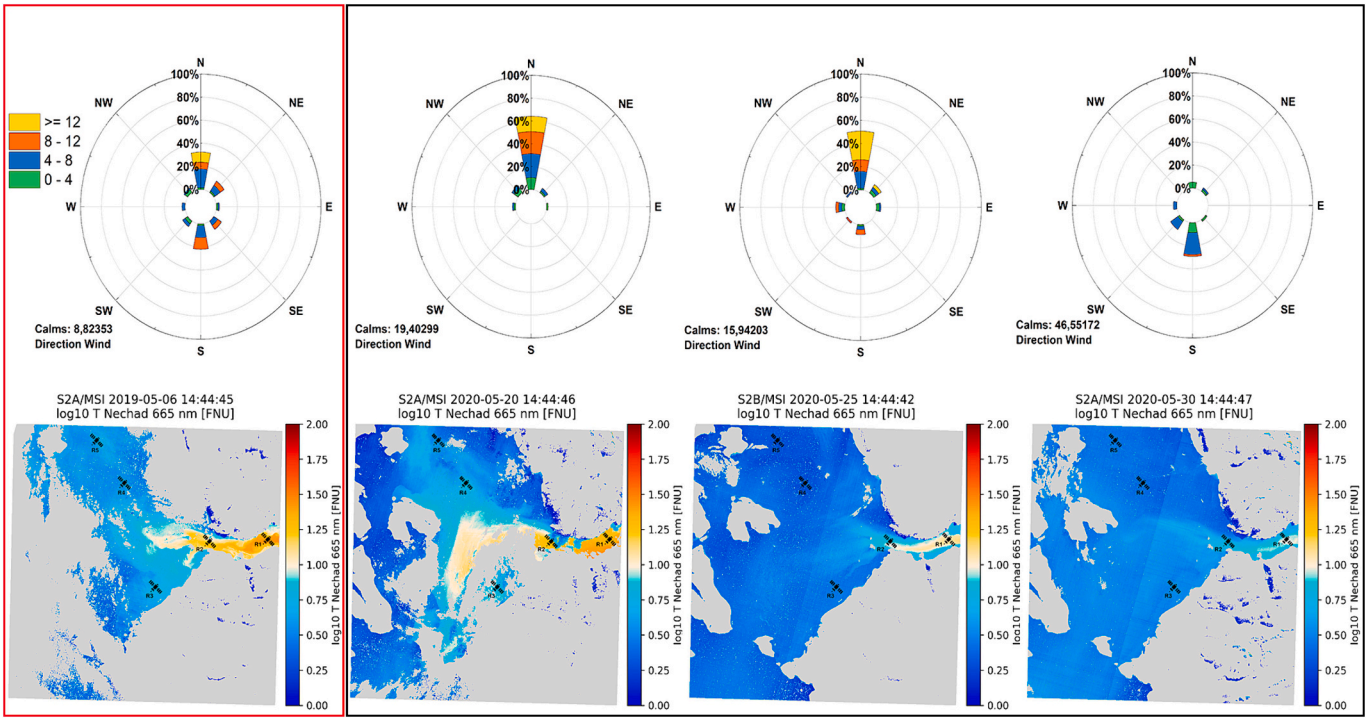

Fig. 8. The top panel shows wind rose corresponding to 72 h before S2 image acquisition and the bottom panel shows results from the Nv09 algorithm for autumn days. The panel in red shows the image from the date with the highest turbidity in 2019-May-06. The panel in black shows the images from 2020-May-20, 2020-May-25, and 2020-May-30, respectively. (For interpretation of the references to color in this figure legend, the reader is referred to the web version of this article.)

et al. (2021), Rodríguez-López et al. (2022). This suggests that winds could be transferring SS, CDOM, and particulate matter from the river discharge and coastal zone to R4 and R5, thus increasing turbidity at both seaward sites.

Several studies have shown that anthropogenic activities, such as land use and land use change (LULUC), aquaculture, and marine traffic, can have a significant impact on water quality in NP (Curra-Sánchez et al., 2022, 2024; Lara et al., 2018; León-Muñoz et al., 2021; Pérez et al., 2015). Organic matter, suspended solids, and other compounds may be present in the environment, including silica, phosphate, nitrite, or nitrate (Paudel et al., 2016; Pérez et al., 2015). Earlier studies have demonstrated that basins that are predominantly influenced by agriculture or native forests can affect and/or modify the size of the solids and the amount of CDOM present in the ecosystem (Alvado et al., 2021; Babin et al., 2003; Curra-Sánchez et al., 2022, 2024; Gippel, 1995). Hence, land-use patterns can also affect the turbidity of coastal water. For example, Curra-Sánchez et al. (2022) observed that runoff from a basin dominated by agricultural use had a greater availability and quantity of nutrients, specifically nitrates and phosphates. In contrast, a basin with a larger area of native forest registered high values of CDOM and lower nutrient concentrations. Surface runoff can contribute large amounts of organic matter and nutrients, such as agricultural or forestry wastes, causing water turbidity to increase due to algal blooms and even HABs on the surface and in the water column (Bilotta and Brazier, 2008; Doan et al., 2015; Hudson and Vandergucht, 2015; Pérez-Ruzafa et al., 2019). Further effects of turbid waters include impacts on benthic and pelagic species, including both photosynthesis-dependent and filter-feeding organisms. Seasonal exposure to turbid waters can disrupt and/or alter the status and growth behavior of these organisms over time and particularly in their early life stages (Alma et al., 2023; Goldsmith et al., 2021). Considering that aquaculture is the main economic activity in the Reloncaví area, the hypotheses tested by our study are highly relevant for the future development of continuous monitoring and warning systems that can reliably detect increases in water turbidity in near-real time. The dynamic spatio-temporal variability of turbidity in the Reloncaví sound underscores the need for comprehensive monitoring strategies to understand and manage WQP in the study area.

4.1. Future directions

More recent studies have estimated turbidity with different Machine Learning (ML) techniques and Ensemble Learning (EL) models, such as Random Forest (RF), feedforward neural network (FNN), Artificial Neural Networks (ANNs), multivariate adaptive regression splines (MARS), Classification and Regression Tree (CART), Extreme Gradient Boosting (XGBoost), Gradient Boosting Decision Tree (GBDT), LightGBM (LGBM), and CatBoost. These new ML approaches have been able to incorporate different environmental variables and water quality parameters, such as land use and land use change, turbidity, pH, chlorophyll, conductivity, precipitation, and temperature, among others (Anmala and Turuganti, 2021; Venkateswarlu and Anmala, 2023; Zhang et al., 2024).

In a basin in Kentucky, USA, Venkateswarlu and Anmala (2023) predicted turbidity by applying RF and FNN. The R^2 prediction of RF for training, testing, and overall was the lowest compared to all other variables tested, while a slightly lower prediction was obtained with FNN (Venkateswarlu and Anmala, 2023). However, Venkateswarlu and Anmala (2023) highlight that the main predictor variables for turbidity were precipitation and temperature. Including both variables (precipitation and temperature) provided a good fit and removing them decreased model performance (Anmala and Turuganti, 2021; Venkateswarlu and Anmala, 2023). The latter results support the correspondence between precipitation and turbid water events in our study and highlights the challenges ahead in the implementation of ML learning approaches in a data-poor environment. The impact of LULUC can directly influence WQP (Curra-Sánchez et al., 2022, 2024). Rivers, connecting terrestrial and marine ecosystems, transport material and solids originating from adjacent basins. In this way, beyond precipitation and temperature, land use patterns should also be considered in turbidity prediction when utilizing ML algorithms (Anmala and

Turuganti, 2021; Venkateswarlu and Anmala, 2023).

In this way, the predictive ability of ML algorithms will certainly improve the prediction and estimation of WQP. Their use in combination with *in situ* and remote sensing observations is poised to help the conservation and management of coastal and aquatic ecosystems, and support decision-making. However, as more data becomes available in the future, new challenges will arise through limited processing time and computational power, together with the complex process of hyperparameter calibration in some ML algorithms.

5. Conclusion

Our study successfully assessed the spatial and temporal correspondence of the ACOLITE turbidity algorithms in the NP marine ecosystem for the first time. Our findings indicate that the Nv09 algorithm is more reliable than the Nv16 algorithm at a wavelength of 665 nm for the development of a future turbidity predictor model in Reloncaví sound. Precipitation-driven river discharge influenced turbidity with a seasonal signal peaking during austral autumn (May). Site R1 (river) and R5 (away from the influence of river discharges) recorded the highest and lowest turbidity values, respectively. However, there is still uncertainty regarding the influence by chlorophyll, suspended solids, and colored dissolved organic matter. More accurate estimates of these parameters will depend on additional *in situ* sampling, the use of alternative spectral bands, and the application of other algorithms. By validating a time series of high-resolution S2 observations with *in situ* data observations around NP, our study contributes to the development of an early warning system that can anticipate the occurrence of high turbidity events and promote future actions that encourage sustainable management of the coastal zone.

Author contributions

Conceptualization: W.G-T., C.L., and B.R.B.; methodology: W.G-T., E.C-S., C.L., EP.U., L.G.-R., J.D., B.R.B.; software: W.G-T., E.C-S. and L.G.-R.; validation: W.G-T., E.C-S. and L.G.-R.; formal analysis: W.G-T.; data curation: W.G-T. and L.G.-R.; writing-original draft preparation: W.G-T.; visualization: W.G-T., E.C-S., and L.G.-R.; supervision: C.L., J.D, and B.R.B. All authors participated in the writing-review, editing, and discussion of the manuscript. All authors have read and agreed to the published version of the manuscript.

Funding

This work was funded by the Data Observatory Foundation, ANID Technology Center No. DO210001.

Declaration of competing interest

The authors declare no conflicts of interest. The authors declare that they have no known competing financial interests or personal relationships that could have appeared to influence the work reported in this paper.

Data availability

The data presented in this study are available on request from the corresponding author. The data are additionally accessible in the Zenodo repository (https://zenodo.org/doi/10.5281/zenodo.13645864).

Acknowledgments

W.G-T. acknowledges to BECA Dirección de Postgrado UCSC; Fondo de Investigación Estratégica en Sequía - ANID grant FSEQ210030 and the Data Observatory Foundation, ANID Technology Center No. DO210001. Thanks to the DO staff and team for their support in preparing and carrying out this work. E.C-S. acknowledges to Fondo Nacional de Desarrollo Científico y Tecnológico de Postdoctorado (ANID-FONDECYT-Postdoctoral 3240540), Dirección de Investigación UDLA, and NIDS. C.L. has been supported by FONDECYT 1230420. L.G.-R. thanks NIDS and the supercomputing infrastructure of the NLHPC (ECM-02) of the Universidad de Chile. B.R.B. is supported by FONDECYT 1221699. The authors express their gratitude to all those who contributed to the publication of this work. All authors are grateful for the online monitoring networks and satellites, such as those of Observatorio Marítimo Reloncaví (OMARE), Dirección General de Aguas (DGA), Chilean Meteorological Directorate (DMC), and the Copernicus programs. The authors thank the editor, associate editor, and reviewers for their time and constructive feedback.

Appendix A. Supplementary data

Supplementary data to this article can be found online at https://doi.org/10.1016/j.ecoinf.2024.102814.

References

Aavaste, A., Sipelgas, L., Uiboupin, R., Uudeberg, K., 2021. Impact of thermohaline conditions on vertical variability of optical properties in the Gulf of Finland (Baltic Sea): implications for water quality remote sensing. Front. Mar. Sci. 8, 537. https://doi.org/10.3389/FMARS.2021.674065/.

Abirhire, O., Davies, J.M., Guo, X., Hudson, J., 2020. Understanding the factors associated with long-term reconstructed turbidity in Lake Diefenbaker from Landsat-imagery. Sci. Total Environ. 724 https://doi.org/10.1016/J.SCITOTENV.2020.138222.

Aguayo, R., León-Muñoz, J., Vargas-Baecheler, J., Montecinos, A., Garreaud, R., Urbina, M., Soto, D., Iriarte, J.L., 2019. The glass half-empty: climate change drives lower freshwater input in the coastal system of the Chilean Northern Patagonia. Clim. Chang. 155 (3), 417–435. https://doi.org/10.1007/S10584-019-02495-6.

Alma, L., Fiamengo, C.J., Alin, S.R., Jackson, M., Hiromoto, K., Padilla-Gamiño, J.L., 2023. Physiological responses of scallops and mussels to environmental variability: implications for future shellfish aquaculture. Mar. Pollut. Bull. 194, 115356 https://doi.org/10.1016/J.MARPOLBUL.2023.115356.

Alvado, B., Sòria-Perpinyà, X., Vicente, E., Delegido, J., Urrego, P., Ruiz-Verdú, A., Soria, J.M., Moreno, J., 2021. Estimating organic and inorganic part of suspended solids from sentinel 2 in different inland waters. Water (Switzerland) 13. https://doi.org/10.3390/W13182453.

Anderson, C.W., 2005. Turbidity (ver.2.1): U.S. Geological Survey Techniques of Water-Resources Investigations, Book 9, Chap. A6, Sec 6.7. Techniques of Water-Resources Investigations, Reston, VA. https://doi.org/10.3133/twri09A6.7.

Anderson, D.M., Cembella, A.D., Hallegraeff, G.M., 2012. Progress in understanding harmful algal blooms: paradigm shifts and new technologies for research, monitoring, and management. Annu. Rev. Mar. Sci. 4, 143–176. https://doi.org/10.1146/ANNUREV-MARINE-120308-081121.

Anmala, J., Turuganti, V., 2021. Comparison of the performance of decision tree (DT) algorithms and extreme learning machine (ELM) model in the prediction of water quality of the upper Green River watershed. Water Environ. Res. 93, 2360–2373. https://doi.org/10.1002/WER.1642.

Aragonés, L., Pagán, J.I., López, M.P., García-Barba, J., 2016. The impacts of Segura River (Spain) channelization on the coastal seabed. Sci. Total Environ. 543, 493–504. https://doi.org/10.1016/j.scitotenv.2015.11.058.

Astorga, M.P., Vargas, J., Valenzuela, A., Molinet, C., Marín, S.L., 2018. Population genetic structure and differential selection in mussel *Mytilus chilensis*. Aquac. Res. 49, 919–927. https://doi.org/10.1111/ARE.13538.

Babin, M., Stramski, D., Ferrari, G.M., Claustre, H., Bricaud, A., Obolensky, G., Hoepffner, N., 2003. Variations in the light absorption coefficients of phytoplankton, nonalgal particles, and dissolved organic matter in coastal waters around Europe. J. Geophys. Res. Oceans 108. https://doi.org/10.1029/2001JC000882.

Balasubramanian, S.V., Pahlevan, N., Smith, B., Binding, C., Schalles, J., Loisel, H., Gurlin, D., Greb, S., Alikas, K., Randla, M., Bunkei, M., Moses, W., Nguyễn, H., Lehmann, M.K., O'Donnell, D., Ondrusek, M., Han, T.H., Fichot, C.G., Moore, T., Boss, E., 2020. Robust algorithm for estimating total suspended solids (TSS) in inland and nearshore coastal waters. Remote Sens. Environ. 246 https://doi.org/10.1016/J.RSE.2020.111768.

Banas, D., Grillas, P., Auby, I., Lescuyer, F., Coulet, E., Moreteau, J.C., Millet, B., 2005. Short time scale changes in underwater irradiance in a wind-exposed lagoon (Vaccarès lagoon, France): efficiency of infrequent field measurements of water turbidity or weather data to predict irradiance in the water column. Hydrobiologia 551, 3–16. https://doi.org/10.1007/S10750-005-4446-1.

Barragán, J.M., de Andrés, M., 2015. Analysis and trends of the world's coastal cities and agglomerations. Ocean Coast. Manag. 114, 11–20. https://doi.org/10.1016/J.OCECOAMAN.2015.06.004.

Barria, A., Gebauer, P., Molinet, C., 2012. Variabilidad espacial y temporal del suministro larval de mitílidos en el Seno de Reloncaví, sur de Chile. Rev. Biol. Mar. Oceanogr. 47, 461–473. https://doi.org/10.4067/s0718-19572012000300009.

Bilotta, G.S., Brazier, R.E., 2008. Understanding the influence of suspended solids on water quality and aquatic biota. Water Res. 42, 2849–2861. https://doi.org/10.1016/J.WATRES.2008.03.018.

Brando, V.E., Braga, F., Zaggia, L., Giardino, C., Bresciani, M., Matta, E., Bellafiore, D., Ferrarin, C., Maicu, F., Benetazzo, A., Bonaldo, D., Falcieri, F.M., Coluccelli, A., Russo, A., Carniel, S., 2015. High-resolution satellite turbidity and sea surface temperature observations of river plume interactions during a significant flood event. Ocean Sci. 11, 909–920. https://doi.org/10.5194/OS-11-909-2015.

Budhiman, S., Suhyb Salama, M., Vekerdy, Z., Verhoef, W., 2012. Deriving optical properties of Mahakam Delta coastal waters, Indonesia using in situ measurements and ocean color model inversion. ISPRS J. Photogramm. Remote Sens. 68, 157–169. https://doi.org/10.1016/J.ISPRSJPRS.2012.01.008.

Buschmann, A., Cabello, F., Young, K., Carvajal, J., Varela, D.A., Henríquez, L., 2009. Salmon aquaculture and coastal ecosystem health in Chile: analysis of regulations, environmental impacts and bioremediation systems. Ocean Coast. Manag. 52, 243–249. https://doi.org/10.1016/J.OCECOAMAN.2009.03.002.

Buschmann, A., Niklitschek, E.J., Pereda, S.V., 2021. Aquaculture and its impacts on the conservation of Chilean Patagonia. In: Castilla, J.C., Armesto, J.J., Martínez-Harms, M.J. (Eds.), Conservación En La Patagonia Chilena: Evaluación Del Conocimiento. Ediciones Universidad Católica, Santiago, Chile, Oportunidades y Desafíos, p. 600.

Caballero, I., Stumpf, R.P., 2020. Towards routine mapping of shallow bathymetry in environments with variable turbidity: contribution of sentinel-2A/B satellites mission. Remote Sens. 12 https://doi.org/10.3390/RS12030451.

Caballero, I., Steinmetz, F., Navarro, G., 2018. Evaluation of the first year of operational sentinel-2A data for retrieval of suspended solids in medium- to high-turbidity waters. Remote Sens. 10 https://doi.org/10.3390/RS10070982.

Caballero, I., Ruiz, J., Navarro, G., 2019. Sentinel-2 satellites provide near-real time evaluation of catastrophic floods in the West Mediterranean. Water (Switzerland) 11. https://doi.org/10.3390/W11122499.

Caballero, I., Fernández, R., Escalante, O.M., Mamán, L., Navarro, G., 2020. New capabilities of sentinel-2A/B satellites combined with in situ data for monitoring small harmful algal blooms in complex coastal waters. Sci. Rep. 10 https://doi.org/10.1038/S41598-020-65600-1.

Caballero, I., Roca, M., Santos-Echeandía, J., Bernárdez, P., Navarro, G., 2022. Use of the Sentinel-2 and Landsat-8 satellites for water quality monitoring: an early warning tool in the mar Menor coastal lagoon. Remote Sens. 14, 2744. https://doi.org/10.3390/RS14122744/.

Camelo-Guarín, S., Molinet, C., Soto, D., 2021. Recommendations for implementing integrated multitrophic aquaculture in commercial farms at the landscape scale in southern Chile. Aquaculture 544, 737116. https://doi.org/10.1016/J.AQUACULTURE.2021.737116.

Castillo, M.I., Cifuentes, U., Pizarro, O., Djurfeldt, L., Caceres, M., 2016. Seasonal hydrography and surface outflow in a fjord with a deep sill: the Reloncaví fjord, Chile. Ocean Sci. 12, 533–534. https://doi.org/10.5194/os-12-533-2016.

Chowdhury, M., Vilas, C., van Bergeijk, S., Navarro, G., Laiz, I., Caballero, I., 2023. Monitoring turbidity in a highly variable estuary using sentinel 2-a/B for ecosystem management applications. Front. Mar. Sci. 10, 1186441 https://doi.org/10.3389/FMARS.2023.1186441/BIBTEX.

Ciancia, E., Campanelli, A., Lacava, T., Palombo, A., Pascucci, S., Pergola, N., Pignatti, S., Satriano, V., Tramutoli, V., 2020. Modeling and multi-temporal characterization of total suspended matter by the combined use of sentinel 2-MSI and landsat 8-OLI data: the Pertusillo lake case study (Italy). Remote Sens. 12 https://doi.org/10.3390/RS12132147.

Cloern, J.E., 1987. Turbidity as a control on phytoplankton biomass and productivity in estuaries. Cont. Shelf Res. 7, 1367–1381. https://doi.org/10.1016/0278-4343(87)90042-2.

Curra-Sánchez, E.D., Lara, C., Cornejo-D'Ottone, M., Nimptsch, J., Aguayo, M., Broitman, B.R., Saldías, G.S., Vargas, C.A., 2022. Contrasting land-uses in two small river basins impact the colored dissolved organic matter concentration and carbonate system along a river-coastal ocean continuum. Sci. Total Environ. 806, 150435 https://doi.org/10.1016/J.SCITOTENV.2021.150435.

Curra-Sánchez, E.D., Valerio, A.D.M., Lara, C., García-Tuñon, W., Broitman, B.R., Saldías, G.S., Nimptsch, J., Vargas, C.A., 2024. CDOM dynamics in two coastal zones influenced by contrasting land uses in northern Patagonia. Estuar. Coast. Shelf Sci. 306, 108897 https://doi.org/10.1016/J.ECSS.2024.108897.

Davies-Colley, R.J., Smith, D.G., 2001. Turbidity, suspended sediment, and water clarity: a review. JAWRA J. Am. Water Resourc. Assoc. 37, 1085–1101. https://doi.org/10.1111/J.1752-1688.2001.TB03624.X.

de Castro Medeiros, L., Mattos, A., Lürling, M., Becker, V., 2015. Is the future blue-green or brown? The effects of extreme events on phytoplankton dynamics in a semi-arid man-made lake. Aquat. Ecol. 49, 293–307. https://doi.org/10.1007/S10452-015-9524-5/FIGURES/8.

Delegido, J., Urrego, P., Vicente, E., Sòria-Perpinyà, X., Soria, J.M., Pereira-Sandoval, M., Ruiz-Verdú, A., Peña, R., Moreno, J., 2019. Turbidity and Secchi disc depth with Sentinel-2 in different trophic status reservoirs at the Comunidad Valenciana. Revista de Teledetección 2019, 15–24. https://doi.org/10.4995/RAET.2019.12603.

Díaz, P.A., Figueroa, R.I., 2023. Toxic algal bloom recurrence in the era of global change: lessons from the Chilean Patagonian fjords. Microorganisms 11, 1874. https://doi.org/10.3390/MICROORGANISMS11081874.

Díaz, P.A., Álvarez, G., Varela, D., Pérez-Santos, I., Díaz, M., Molinet, C., Seguel, M., Aguilera-Belmonte, A., Guzmán, L., Uribe, E., Rengel, J., Hernández, C., Segura, C., Figueroa, R.I., 2019. Impacts of harmful algal blooms on the aquaculture industry: Chile as a case study. Perspect. Phycol. 6, 39–50. https://doi.org/10.1127/PIP/2019/0081.

Dickey, T., Lewis, M., Chang, G., 2006. Optical oceanography: recent advances and future directions using global remote sensing and in situ observations. Rev. Geophys. 44 https://doi.org/10.1029/2003RG000148.

Doan, P.T.K., Némery, J., Schmid, M., Gratiot, N., 2015. Eutrophication of turbid tropical reservoirs: scenarios of evolution of the reservoir of Cointzio, Mexico. Ecol. Inform. 29, 192–205. https://doi.org/10.1016/J.ECOINF.2015.01.006.

Dogliotti, A.I., Ruddick, K.G., Nechad, B., Doxaran, D., Knaeps, E., 2015. A single algorithm to retrieve turbidity from remotely-sensed data in all coastal and estuarine waters. Remote Sens. Environ. 156, 157–168. https://doi.org/10.1016/J.RSE.2014.09.020.

Elhag, M., Gitas, I., Othman, A., Bahrawi, J., Gikas, P., 2019. Assessment of water quality parameters using temporal remote sensing spectral reflectance in arid environments, Saudi Arabia. Water 11, 556. https://doi.org/10.3390/W11030556.

ESA - European Space Agency, 2015. Sentinel-2 User Handbook. ESA Standard Document. European Space Agency, París.

FAO, 2022. The State of World Fisheries and Aquaculture 2022. Towards Blue Transformation. https://doi.org/10.4060/CC0461EN.

Flores, R.P., Lara, C., Saldías, G.S., Vásquez, S.I., Roco, A., 2022. Spatio-temporal variability of turbid freshwater plumes in the Inner Sea of Chiloé, northern Patagonia. J. Mar. Syst. 228, 103709 https://doi.org/10.1016/J.JMARSYS.2022.103709.

Garreaud, R., 2018. Record-breaking climate anomalies lead to severe drought and environmental disruption in western Patagonia in 2016. Clim. Res. 74, 217–229. https://doi.org/10.3354/cr01505.

Garreaud, R., Lopez, P., Minvielle, M., Rojas, M., 2013. Large-scale control on the Patagonian climate. J. Clim. 26, 215–230. https://doi.org/10.1175/jcli-d-12-00001.1.

GEBCO, 2024. Gridded Bathymetry Data [WWW Document]. URL. https://www.gebco.net/data_and_products/gridded_bathymetry_data/ (accessed 4.25.23).

Gelda, R.K., Effler, S.W., Prestigiacomo, A.R., Peng, F., Effler, A.J.P., Wagner, B.A., Perkins, M.G., O'Donnell, D.M., O'Donnell, S.M., Pierson, D.C., 2013. Characterizations and modeling of turbidity in a water supply reservoir following an extreme runoff event. Inland Waters 3, 377–390. https://doi.org/10.5268/IW-3.3.581.

Gippel, C.J., 1995. Potential of turbidity monitoring for measuring the transport of suspended solids in streams. Hydrol. Process. 9 (1), 83–97. https://doi.org/10.1002/HYP.3360090108.

Goldsmith, A.M., Jaber, F.H., Ahmari, H., Randklev, C.R., 2021. Clearing up cloudy waters: a review of sediment impacts to unionid freshwater mussels. Environ. Rev. 29 (1), 100–108.

Grobbelaar, J.U., 2009. Turbidity. In: Encyclopedia of Inland Waters, pp. 699–704. https://doi.org/10.1016/B978-012370626-3.00075-2.

Harmel, T., Chami, M., Tormos, T., Reynaud, N., Danis, P.A., 2018. Sunglint correction of the multi-spectral instrument (MSI)-SENTINEL-2 imagery over inland and sea waters from SWIR bands. Remote Sens. Environ. 204, 308–321. https://doi.org/10.1016/J.RSE.2017.10.022.

Hudson, J.J., Vandergucht, D.M., 2015. Spatial and temporal patterns in physical properties and dissolved oxygen in Lake Diefenbaker, a large reservoir on the Canadian prairies. J. Great Lakes Res. 41, 22–33. https://doi.org/10.1016/J.JGLR.2015.06.007.

Huettmann, F., Arhonditsis, G., 2023. Towards an ecological informatics scholarship that is reflective, repeatable, transparent, and sharable! Ecol. Inform. 76, 102132 https://doi.org/10.1016/J.ECOINF.2023.102132.

Hyun, J.C., 2007. Effects of prevailing winds on turbidity of a shallow estuary. Int. J. Environ. Res. Public Health 4, 185–192. https://doi.org/10.3390/IJERPH2007040014.

Iriarte, J.L., González, H.E., Liu, K.K., Rivas, C., Valenzuela, C., 2007. Spatial and temporal variability of chlorophyll and primary productivity in surface waters of southern Chile (41.5–43°S). Estuar. Coast. Shelf Sci. 74, 471–480. https://doi.org/10.1016/J.ECSS.2007.05.015.

Iriarte, J.L., Pantoja, S., Daneri, G., Iriarte, J.L., Pantoja, S., Daneri, G., 2014. Oceanographic processes in Chilean fjords of Patagonia: from small to large-scale studies. Prog. Oceanogr. 129, 1–7. https://doi.org/10.1016/J.POCEAN.2014.10.004.

Iriarte, J.L., León-Muñoz, J., Marcé, R., Clément, A., Lara, C., 2017. Influence of seasonal freshwater streamflow regimes on phytoplankton blooms in a Patagonian fjord. New Zeal. J. Mar. Freshw. Res. 51, 304–315. https://doi.org/10.1080/00288330.2016.1220955.

Jerlov, N.G., 1957. A transparency-meter for ocean water. Tellus 9, 229–233. https://doi.org/10.1111/J.2153-3490.1957.TB01877.X.

Jiang, J., Chen, Z., Sun, K., Chen, Y., Mu, M., Sun, Q., Zeng, S., 2024. Monitoring 36-year water clarity dynamics in turbid waters of the Pearl River estuary, China, using Landsat data. Ecol. Inform. 81, 102600 https://doi.org/10.1016/J.ECOINF.2024.102600.

Khan, R.M., Salehi, B., Mahdianpari, M., Mohammadimanesh, F., Mountrakis, G., Quackenbush, L.J., 2021. A meta-analysis on harmful algal bloom (HAB) detection and monitoring: a remote sensing perspective. Remote Sens. 13, 4347. https://doi.org/10.3390/RS13214347.

Kirk, J.T.O., 1984. Dependence of relationship between inherent and apparent optical properties of water on solar altitude. Limnol. Oceanogr. 29, 350–356. https://doi.org/10.4319/LO.1984.29.2.0350.

Kirk, J.T.O., 1985. Effects of suspensoids (turbidity) on penetration of solar radiation in aquatic ecosystems. Hydrobiologia 125, 195–208. https://doi.org/10.1007/BF00045935.

Kuhn, C., de Matos Valerio, A., Ward, N., Loken, L., Sawakuchi, H.O., Kampel, M., Richey, J., Stadler, P., Crawford, J., Striegl, R., Vermote, E., Pahlevan, N.,

Butman, D., 2019. Performance of Landsat-8 and Sentinel-2 surface reflectance products for river remote sensing retrievals of chlorophyll-a and turbidity. Remote Sens. Environ. 224, 104–118. https://doi.org/10.1016/j.rse.2019.01.023.
Lara, A., Villalba, R., Urrutia, R., 2008. A 400-year tree-ring record of the Puelo River summer-fall streamflow in the Valdivian rainforest eco-region, Chile. Clim. Chang. 86, 331–356. https://doi.org/10.1007/S10584-007-9287-7/METRICS.
Lara, C., Miranda, M., Montecino, V., Iriarte, J.L., 2010. Chlorophyll-a MODIS mesoscale variability in the Inner Sea of Chiloé, Patagonia, Chile (41-43°S): patches and gradients? Rev. Biol. Mar. Oceanogr. 45, 217–225. https://doi.org/10.4067/S0718-19572010000200003.
Lara, C., Saldías, G.S., Tapia, F.J., Iriarte, J.L., Broitman, B.R., 2016. Interannual variability in temporal patterns of chlorophyll–a and their potential influence on the supply of mussel larvae to inner waters in northern Patagonia (41–44°S). J. Mar. Syst. 155, 11–18. https://doi.org/10.1016/J.JMARSYS.2015.10.010.
Lara, C., Saldías, G.S., Paredes, A.L., Cazelles, B., Broitman, B.R., 2018. Temporal variability of MODIS Phenological indices in the temperate rainforest of northern Patagonia. Remote Sens. 10, 956. https://doi.org/10.3390/RS10060956.
Lee, Z., Carder, K.L., Arnone, R.A., 2002. Deriving inherent optical properties from water color: a multiband quasi-analytical algorithm for optically deep waters. Appl. Opt. 41 (27), 5755–5772. https://doi.org/10.1364/AO.41.005755.
Lee, H.W., Kim, E.J., Park, S.S., Choi, J.H., 2015. Effects of climate change on the movement of turbidity flow in a stratified reservoir. Water Resour. Manag. 29, 4095–4110. https://doi.org/10.1007/S11269-015-1047-2/FIGURES/7.
León-Muñoz, J., Marcé, R., Iriarte, J.L., 2013. Influence of hydrological regime of an Andean river on salinity, temperature and oxygen in a Patagonia fjord, Chile. New Zeal. J. Mar. Freshw. Res. 47, 515–528. https://doi.org/10.1080/00288330.2013.802700.
León-Muñoz, J., Urbina, M.A., Garreaud, R., Iriarte, J.L., 2018. Hydroclimatic conditions trigger record harmful algal bloom in western Patagonia (summer 2016). Sci. Rep. 8, 1330. https://doi.org/10.1038/s41598-018-19461-4.
León-Muñoz, J., Aguayo, R., Marcé, R., Catalán, N., Woelfl, S., Nimptsch, J., Arismendi, I., Contreras, C., Soto, D., Miranda, A., 2021. Climate and land cover trends affecting freshwater inputs to a fjord in northwestern Patagonia. Front. Mar. Sci. 8, 960. https://doi.org/10.3389/FMARS.2021.628454/BIBTEX.
Lizcano-Sandoval, L., Anastasiou, C., Montes, E., Raulerson, G., Sherwood, E., Muller-Karger, F.E., 2022. Seagrass distribution, areal cover, and changes (1990–2021) in coastal waters off west-Central Florida, USA. Estuar. Coast. Shelf Sci. 279, 108134 https://doi.org/10.1016/J.ECSS.2022.108134.
Magrì, S., Ottaviani, E., Prampolini, E., Federici, B., Besio, G., Fabiano, B., 2023. Application of machine learning techniques to derive sea water turbidity from Sentinel-2 imagery. Remote Sens. Appl. 30, 100951 https://doi.org/10.1016/J.RSASE.2023.100951.
Mahmoud, S.H., Ahmed, S., Zhu, D.Z., Gan, T.Y., Loewen, M.R., van Duin, B., Mahmood, K., 2023. Monitoring the spatial distribution of water quality of an urban stormwater pond using satellite images. Ecol. Inform. 77, 102205 https://doi.org/10.1016/J.ECOINF.2023.102205.
Mélin, F., Vantrepotte, V., 2015. How optically diverse is the coastal ocean? Remote Sens. Environ. 160, 235–251. https://doi.org/10.1016/J.RSE.2015.01.023.
Mendes, R., Vaz, N., Fernández-Nóvoa, D., Da Silva, J.C.B., DeCastro, M., Gómez-Gesteira, M., Dias, J.M., 2014. Observation of a turbid plume using MODIS imagery: the case of Douro estuary (Portugal). Remote Sens. Environ. 154, 127–138. https://doi.org/10.1016/J.RSE.2014.08.003.
Mobley, C.D., 2001. Radiative Transfer in the Ocean. Encyclopedia of Ocean Sciences, pp. 2321–2330. https://doi.org/10.1006/RWOS.2001.0469.
Mobley, C.D., 2022. The oceanic optics book. In: International Ocean Colour Coordinating Group (IOCCG). Dartmouth, NS, Canada, p. 924. https://doi.org/10.25607/OBP-1710.
Molinet, C., Díaz Gomez, M.A., Arriagada Muñoz, C.B., Cares Pérez, L.E., Marín Arribas, S.L., Astorga Opazo, M.P., Niklitschek Huaquin, E.J.E., 2015. Spatial distribution pattern of *Mytilus chilensis* beds in the Reloncaví fjord: hypothesis on associated processes. Rev. Chil. Hist. Nat. 88, 1–12. https://doi.org/10.1186/S40693-015-0041-7/.
Molinet, C., Astorga, M., Cares, L., Diaz, M., Hueicha, K., Marín, S., Matamala, T., Soto, D., 2021. Vertical distribution patterns of larval supply and spatfall of three species of Mytilidae in a Chilean fjord used for mussel farming: insights for mussel spatfall efficiency. Aquaculture 535, 736341. https://doi.org/10.1016/J.AQUACULTURE.2021.736341.
Morel, A., Gentili, B., 1993. Diffuse reflectance of oceanic waters II bidirectional aspects. Appl. Opt. 32, 6864. https://doi.org/10.1364/AO.32.006864.
Morel, A., Prieur, L., 1977. Analysis of variations in ocean color. Limnol. Oceanogr. 22, 709–722. https://doi.org/10.4319/LO.1977.22.4.0709.
Nechad, B., Ruddick, K.G., Neukermans, G., 2009. Calibration and validation of a generic multisensor algorithm for mapping of turbidity in coastal waters. Remote Sens. Ocean Sea Ice Large Water Regions 2009 (7473), 74730H. https://doi.org/10.1117/12.830700.
Nechad, B., Ruddick, K.G., Park, Y., 2010. Calibration and validation of a generic multisensor algorithm for mapping of total suspended matter in turbid waters. Remote Sens. Environ. 114, 854–866. https://doi.org/10.1016/J.RSE.2009.11.022.
Nechad, B., Dogliotti, A., Ruddick, K., Doxaran, D., 2016. Particulate backscattering retrieval from remotely-sensed turbidity in various coastal and riverine turbid waters. In: Proceedings of ESA Living Planet Symposium, Prague, 9–13 May 2016, ESA-SP, p. 740. https://odnature.naturalsciences.be/downloads/publications/1241nechad_with_header75.pdf.
Newell, C.R., Hawkins, A.J.S., Morris, K., Boss, E., Thomas, A.C., Kiffney, T.J., Brady, D. C., 2021. Using High-Resolution Remote Sensing to Characterize Suspended Particulate Organic Matter as Bivalve Food for Aquaculture Site Selection, 40, pp. 113–118. https://doi.org/10.2983/035.040.0110.
Novoa, S., Doxaran, D., Ody, A., Vanhellemont, Q., Lafon, V., Lubac, B., Gernez, P., 2017. Atmospheric corrections and multi-conditional algorithm for multi-sensor remote sensing of suspended particulate matter in low-to-high turbidity levels coastal waters. Remote Sens. 9 https://doi.org/10.3390/RS9010061.
Odermatt, D., Gitelson, A., Brando, V.E., Schaepman, M., 2012. Review of constituent retrieval in optically deep and complex waters from satellite imagery. Remote Sens. Environ. 118, 116–126. https://doi.org/10.1016/J.RSE.2011.11.013.
Pahlevan, N., Smith, B., Binding, C., O'Donnell, D.M., 2017. Spectral band adjustments for remote sensing reflectance spectra in coastal/inland waters. Opt. Express 25, 28650. https://doi.org/10.1364/OE.25.028650.
Pahlevan, N., Mangin, A., Balasubramanian, S.V., Smith, B., Alikas, K., Arai, K., Barbosa, C., Bélanger, S., Binding, C., Bresciani, M., Giardino, C., Gurlin, D., Fan, Y., Harmel, T., Hunter, P., Ishikaza, J., Kratzer, S., Lehmann, M.K., Ligi, M., Ma, R., Martin-Lauzer, F.R., Olmanson, L., Oppelt, N., Pan, Y., Peters, S., Reynaud, N., Sander de Carvalho, L.A., Simis, S., Spyrakos, E., Steinmetz, F., Stelzer, K., Sterckx, S., Tormos, T., Tyler, A., Vanhellemont, Q., Warren, M., 2021. ACIX-aqua: a global assessment of atmospheric correction methods for Landsat-8 and Sentinel-2 over lakes, rivers, and coastal waters. Remote Sens. Environ. 258 https://doi.org/10.1016/J.RSE.2021.112366.
Pantoja, S., Iriarte, J.L., Daneri, G., 2011. Oceanography of the Chilean Patagonia. Cont. Shelf Res. 31, 149–153. https://doi.org/10.1016/J.CSR.2010.10.013.
Paudel, B., Velinsky, D., Belton, T., Pang, H., 2016. Spatial variability of estuarine environmental drivers and response by phytoplankton: a multivariate modeling approach. Ecol. Inform. 34, 1–12. https://doi.org/10.1016/J.ECOINF.2016.04.013.
Paulista, R.S.D., de Almeida, F.T., de Souza, A.P., Hoshide, A.K., de Abreu, D.C., da Silva Araujo, J.W., Martim, C.C., 2023. Estimating suspended sediment concentration using remote sensing for the Teles Pires River. Brazil. Sustainability 15, 7049. https://doi.org/10.3390/SU15097049.
Pérez, C.A., DeGrandpre, M.D., Lagos, N.A., Saldías, G.S., Cascales, E.K., Vargas, C.A., 2015. Influence of climate and land use in carbon biogeochemistry in lower reaches of rivers in central southern Chile: implications for the carbonate system in river-influenced rocky shore environments. J. Geophys. Res. Biogeosci. 120, 673–692. https://doi.org/10.1002/2014JG002699.
Pérez-Ruzafa, A., Campillo, S., Fernández-Palacios, J.M., García-Lacunza, A., García-Oliva, M., Ibañez, H., Navarro-Martínez, P.C., Pérez-Marcos, M., Pérez-Ruzafa, I.M., Quispe-Becerra, J.I., Sala-Mirete, A., Sánchez, O., Marcos, C., 2019. Long-term dynamic in nutrients, chlorophyll a, and water quality parameters in a coastal lagoon during a process of eutrophication for decades, a sudden break and a relatively rapid recovery. Front. Mar. Sci. 6, 26. https://doi.org/10.3389/FMARS.2019.00026/BIBTEX.
Pérez-Santos, I., Seguel, R., Schneider, W., Linford, P., Donoso, D., Navarro, E., Amaya-Cárcamo, C., Pinilla, E., Daneri, G., 2019. Synoptic-scale variability of surface winds and ocean response to atmospheric forcing in the eastern austral pacific ocean. Ocean Sci. 15, 1247–1266. https://doi.org/10.5194/OS-15-1247-2019.
Pérez-Santos, I., Díaz, P.A., Silva, N., Garreaud, R., Montero, P., Henríquez-Castillo, C., Barrera, F., Linford, P., Amaya, C., Contreras, S., Aracena, C., Pinilla, E., Altamirano, R., Vallejos, L., Pavez, J., Maulen, J., 2021. Oceanography time series reveals annual asynchrony input between oceanic and estuarine waters in Patagonian fjords. Sci. Total Environ. 798, 149241 https://doi.org/10.1016/J.SCITOTENV.2021.149241.
Phuoc Hoang Son, T., Lau, K., Minh-Thu, P., 2013. The inherent optical properties (IOPs) algorithms for detection the water quality in turbid waters of Mekong estuaries. In: 34th Asian Conference on Remote Sensing 2013, ACRS 2013, 1, pp. 174–180.
Pinilla Matamala, E., 2011. Informe Final. Convenio asesoría integral para la toma de Decisiones en pesca y Acuicultura. Determinación de las condiciones oceanográficas en las áreas Seno de Reloncaví y mar interior de Chiloé. Instituto de Fomento Pesquero.
Potes, M., Costa, M.J., Salgado, R., 2012. Satellite remote sensing of water turbidity in Alqueva reservoir and implications on lake modelling. Hydrol. Earth Syst. Sci. 16, 1623–1633. https://doi.org/10.5194/HESS-16-1623-2012.
Preisendorfer, R.W., 1976. Hydrologic Optics, Volumen 1. Introduction. Honululu, Hawaii.
Quang, N.H., Sasaki, J., Higa, H., Huan, N.H., 2017. Spatiotemporal variation of turbidity based on landsat 8 OLI in Cam Ranh Bay and Thuy Trieu Lagoon, Vietnam. Water (Switzerland) 9. https://doi.org/10.3390/W9080570.
Rodríguez-Benito, C.V., Navarro, G., Caballero, I., 2020. Using Copernicus Sentinel-2 and Sentinel-3 data to monitor harmful algal blooms in southern Chile during the COVID-19 lockdown. Mar. Pollut. Bull. 161, 111722 https://doi.org/10.1016/J.MARPOLBUL.2020.111722.
Rodríguez-López, L., González-Rodríguez, L., Duran-Llacer, I., García, W., Cardenas, R., Urrutia, R., 2022. Assessment of the diffuse attenuation coefficient of photosynthetically active radiation in a Chilean Lake. Remote Sens. 14, 4568. https://doi.org/10.3390/RS14184568/S1.
Saldías, G.S., Sobarzo, M., Largier, J., Moffat, C., Letelier, R., 2012. Seasonal variability of turbid river plumes off Central Chile based on high-resolution MODIS imagery. Remote Sens. Environ. 123, 220–233. https://doi.org/10.1016/J.RSE.2012.03.010.
Saldías, G.S., Sobarzo, M., Quiñones, R., 2019. Freshwater structure and its seasonal variability off western Patagonia. Prog. Oceanogr. 174, 143–153. https://doi.org/10.1016/J.POCEAN.2018.10.014.
Saldías, G.S., Hernández, W., Lara, C., Muñoz, R., Rojas, C., Vásquez, S., Pérez-Santos, I., Soto-Mardones, L., 2021. Seasonal variability of SST fronts in the Inner Sea of Chiloé and its adjacent Coastal Ocean, northern Patagonia. Remote Sens. 13, 181. https://doi.org/10.3390/RS13020181.

Sandoval, M., Parada, C., Torres, R., 2018. Proposal of an integrated system for forecasting harmful algal blooms (HAB) in Chile. Lat. Am. J. Aquat. Res. 46, 424–451. https://doi.org/10.3856/VOL46-ISSUE2-FULLTEXT-18.

Shen, M., Wang, S., Li, Y., Tang, M., Ma, Y., 2021. Pattern of turbidity change in the middle reaches of the Yarlung Zangbo River, southern Tibetan plateau, from 2007 to 2017. Remote Sens. 13, 182. https://doi.org/10.3390/RS13020182.

Smith, V.H., 2003. Eutrophication of freshwater and coastal marine ecosystems: a global problem. Environ. Sci. Pollut. Res. 10, 126–139. https://doi.org/10.1065/ESPR2002.12.142.

Snyder, J., Boss, E., Weatherbee, R., Thomas, A.C., Brady, D., Newell, C., 2017. Oyster aquaculture site selection using landsat 8-derived sea surface temperature, turbidity, and chlorophyll a. Front. Mar. Sci. 4, 263366 https://doi.org/10.3389/FMARS.2017.00190/.

Soomets, T., Uudeberg, K., Jakovels, D., Brauns, A., Zagars, M., Kutser, T., 2020. Validation and comparison of water quality products in Baltic Lakes using Sentinel-2 MSI and Sentinel-3 OLCI data. Sensors 20, 742. https://doi.org/10.3390/S20030742.

Soria, J., Jover, M., Domínguez-Gómez, J.A., 2021. Influence of wind on suspended matter in the water of the Albufera of Valencia (Spain). J. Mar. Sci. Eng. 9 https://doi.org/10.3390/JMSE9030343.

Soriano-González, J., Urrego, E.P., Sòria-Perpinyà, X., Angelats, E., Alcaraz, C., Delegido, J., Ruiz-Verdú, A., Tenjo, C., Vicente, E., Moreno, J., 2022. Towards the combination of C2RCC processors for improving water quality retrieval in inland and coastal areas. Remote Sens. 14, 1124. https://doi.org/10.3390/RS14051124.

Sòria-Perpinyà, X., Vicente, E., Urrego, P., Pereira-Sandoval, M., Tenjo, C., Ruiz-Verdú, A., Delegido, J., Soria, J.M., Peña, R., Moreno, J., 2021. Validation of water quality monitoring algorithms for sentinel-2 and sentinel-3 in mediterranean inland waters with in situ reflectance data. Water (Switzerland) 13. https://doi.org/10.3390/W13050686.

Sòria-Perpinyà, X., Delegido, J., Urrego, E.P., Ruiz-Verdú, A., Soria, J.M., Vicente, E., Moreno, J., 2022. Assessment of Sentinel-2-MSI atmospheric correction processors and in situ spectrometry waters quality algorithms. Remote Sens. 14, 4794. https://doi.org/10.3390/RS14194794.

Soto, D., León-Muñoz, J., Dresdner, J., Luengo, C., Tapia, F.J., Garreaud, R., 2019. Salmon farming vulnerability to climate change in southern Chile: understanding the biophysical, socioeconomic and governance links. Rev. Aquac. 11, 354–374. https://doi.org/10.1111/RAQ.12336.

Soto-Mardones, L., Letelier, J., Salinas, S., Pinillas, E., Belmar, J.P., 2009. Analysis of oceanographic and atmospheric parameters of Seno Reloncaví. Gayana (Concepc) 73, 141–155.

Subiabre, A., Rojas, C., 1994. Geografía Física de la Región de Los Lagos.

Sun, X., Liu, J., Wang, J., Tian, L., Zhou, Q., Li, J., 2021. Integrated monitoring of lakes' turbidity in Wuhan, China during the COVID-19 epidemic using multi-sensor satellite observations. Int. J. Digit. Earth 14, 443–463. https://doi.org/10.1080/17538947.2020.1868584.

Tavora, J., Gonçalves, G.A., Fernandes, E.H., Salama, M.S., van der Wal, D., 2023a. Detecting turbid plumes from satellite remote sensing: state-of-art thresholds and the novel PLUMES algorithm. Front. Mar. Sci. 10 https://doi.org/10.3389/FMARS.2023.1215327.

Tavora, J., Jiang, B., Kiffney, T., Bourdin, G., Gray, P.C., de Carvalho, L.S., Hesketh, G., Schild, K.M., de Souza, L.F., Brady, D.C., Boss, E., 2023b. Recipes for the derivation of water quality parameters using the high-spatial-resolution data from sensors on board sentinel-2A, sentinel-2B, Landsat-5, Landsat-7, Landsat-8, and Landsat-9 satellites. J. Remote Sens. (US) 3. https://doi.org/10.34133/REMOTESENSING.0049.

Taylor, K.E., 2001. Summarizing multiple aspects of model performance in a single diagram. J. Geophys. Res. Atmos. 106, 7183–7192. https://doi.org/10.1029/2000JD900719.

Uudeberg, K., Ansko, I., Põru, G., Ansper, A., Reinart, A., 2019. Using optical water types to monitor changes in optically complex inland and coastal waters. Remote Sens. 11 https://doi.org/10.3390/RS11192297.

Uudeberg, K., Aavaste, A., Kõks, K.L., Ansper, A., Uusõue, M., Kangro, K., Ansko, I., Ligi, M., Toming, K., Reinart, A., 2020. Opticalwater type guided approach to estimate optical water quality parameters. Remote Sens. 12. https://doi.org/10.3390/RS12060931.

Valle-Levinson, A., Sarkar, N., Sanay, R., Soto, D., León, J., 2007. Spatial structure of hydrography and flow in a Chilean fjord, Estuario Reloncaví. Estuar. Coasts 30, 113–126. https://doi.org/10.1007/BF02782972/METRICS.

Vanhellemont, Q., 2019. Adaptation of the dark spectrum fitting atmospheric correction for aquatic applications of the Landsat and Sentinel-2 archives. Remote Sens. Environ. 225, 175–192. https://doi.org/10.1016/J.RSE.2019.03.010.

Vanhellemont, Q., 2020. Sensitivity analysis of the dark spectrum fitting atmospheric correction for metre- and decametre-scale satellite imagery using autonomous hyperspectral radiometry. Opt. Express 28 (20), 29948–29965. https://doi.org/10.1364/OE.397456.

Vanhellemont, Q., Ruddick, K., 2014. Turbid wakes associated with offshore wind turbines observed with Landsat 8. Remote Sens. Environ. 145, 105–115. https://doi.org/10.1016/J.RSE.2014.01.009.

Vanhellemont, Q., Ruddick, K., 2016. Acolite for Sentinel-2: Aquatic Applications of MSI Imagery, 740. ESA Special Publication SP.

Vanhellemont, Q., Ruddick, K., 2018. Atmospheric correction of metre-scale optical satellite data for inland and coastal water applications. Remote Sens. Environ. 216, 586–597. https://doi.org/10.1016/J.RSE.2018.07.015.

Vanhellemont, Q., Ruddick, K., 2021. Atmospheric correction of Sentinel-3/OLCI data for mapping of suspended particulate matter and chlorophyll-a concentration in Belgian turbid coastal waters. Remote Sens. Environ. 256, 112284 https://doi.org/10.1016/J.RSE.2021.112284.

Vantrepotte, V., Loisel, H., Dessailly, D., Mériaux, X., 2012. Optical classification of contrasted coastal waters. Remote Sens. Environ. 123, 306–323. https://doi.org/10.1016/J.RSE.2012.03.004.

Vásquez, S.I., Belén De La Torre, M., Saldías, G.S., Montecinos, A., Lausch, A., Bumberger, J., Oppelt, N., 2021. Meridional changes in satellite chlorophyll and fluorescence in optically-complex coastal waters of Northern Patagonia. Remote Sens. 13, 1026. https://doi.org/10.3390/RS13051026.

Venkateswarlu, T., Anmala, J., 2023. Importance of land use factors in the prediction of water quality of the Upper Green River watershed, Kentucky, USA, using random forest. Environ. Dev. Sustain. 1–24. https://doi.org/10.1007/S10668-023-03630-1/.

Vijay Prakash, K., Geetha Vimala, C.S., Preethi Latha, T., Jayaram, C., Nagamani, P.V., Laxmi, C.N.V., 2021. Assessment of water quality along the southeast coast of India during COVID-19 lockdown. Front. Mar. Sci. 8, 338. https://doi.org/10.3389/FMARS.2021.659686/BIBTEX.

Werdell, P.J., McKinna, L.I.W., Boss, E., Ackleson, S.G., Craig, S.E., Gregg, W.W., Lee, Z., Maritorena, S., Roesler, C.S., Rousseaux, C.S., Stramski, D., Sullivan, J.M., Twardowski, M.S., Tzortziou, M., Zhang, X., 2018. An overview of approaches and challenges for retrieving marine inherent optical properties from ocean color remote sensing. Prog. Oceanogr. 160, 186–212. https://doi.org/10.1016/J.POCEAN.2018.01.001.

Zhan, Y., Delegido, J., Erena, M., Soria, J.M., Ruiz-Verdú, A., Urrego, P., Sòria-Perpinyà, X., Vicente, E., Moreno, J., 2022. Mar Menor lagoon (SE Spain) chlorophyll-a and turbidity estimation with Sentinel-2. Limnetica 41, 305–323. https://doi.org/10.23818/LIMN.41.18.

Zhang, J., Meng, F., Fu, P., Jing, T., Xu, J., Yang, X., 2024. Tracking changes in chlorophyll-a concentration and turbidity in Nansi Lake using Sentinel-2 imagery: a novel machine learning approach. Ecol. Inform. 81, 102597 https://doi.org/10.1016/J.ECOINF.2024.102597.

Zohary, T., Padisák, J., Naselli-Flores, L., 2009. Phytoplankton in the physical environment: beyond nutrients, at the end, there is some light. Hydrobiologia 639, 261–269. https://doi.org/10.1007/S10750-009-0032-2.